



# Numerical Simulations of Turbulent Molecular Clouds Regulated by Radiation Feedback Forces. II. Radiation–Gas Interactions and Outflows

Sudhir Raskutti, Eve C. Ostriker , and M. Aaron Skinner

Department of Astrophysical Sciences, Princeton University, Princeton, NJ 08544, USA

Received 2016 July 26; revised 2017 September 7; accepted 2017 October 24; published 2017 November 22

## Abstract

Momentum deposition by radiation pressure from young, massive stars may help to destroy molecular clouds and unbind stellar clusters by driving large-scale outflows. We extend our previous numerical radiation hydrodynamic study of turbulent star-forming clouds to analyze the detailed interaction between non-ionizing UV radiation and the cloud material. Our simulations trace the evolution of gas and star particles through self-gravitating collapse, star formation, and cloud destruction via radiation-driven outflows. These models are idealized in that we include only radiation feedback and adopt an isothermal equation of state. Turbulence creates a structure of dense filaments and large holes through which radiation escapes, such that only  $\sim 50\%$  of the radiation is (cumulatively) absorbed by the end of star formation. The surface density distribution of gas by mass as seen by the central cluster is roughly lognormal with  $\sigma_{\ln \Sigma} = 1.3\text{--}1.7$ , similar to the externally projected surface density distribution. This allows low surface density regions to be driven outwards to nearly 10 times their initial escape speed  $v_{\text{esc}}$ . Although the velocity distribution of outflows is broadened by the lognormal surface density distribution, the overall efficiency of momentum injection to the gas cloud is reduced because much of the radiation escapes. The mean outflow velocity is approximately twice the escape speed from the initial cloud radius. Our results are also informative for understanding galactic-scale wind driving by radiation, in particular, the relationship between velocity and surface density for individual outflow structures and the resulting velocity and mass distributions arising from turbulent sources.

*Key words:* hydrodynamics – ISM: clouds – methods: numerical – radiative transfer – stars: formation

## 1. Introduction

Momentum deposition in giant molecular clouds (GMCs) by radiation from young O stars is often proposed as a means for driving turbulence, propelling high-velocity outflows (Matzner 2002; Goldbaum et al. 2011; Hopkins et al. 2011, 2012; Krumholz & Thompson 2012; Matzner & Jumper 2015; Thompson et al. 2015; Thompson & Krumholz 2016), and eventually causing cloud destruction (O’Dell et al. 1967; Elmegreen 1983; Scoville et al. 2001; Krumholz & Matzner 2009; Fall et al. 2010; Krumholz & Dekel 2010; Murray et al. 2010; Sales et al. 2014; Skinner & Ostriker 2015; Kim et al. 2016; Raskutti et al. 2016). In extreme galactic environments, radiation pressure may play an important role in helping to support the overall interstellar medium (ISM) against gravity (limiting further star formation) and/or launching galactic-scale winds (Harwit 1962; Scoville 2003; Murray et al. 2005; Thompson et al. 2005; Hopkins et al. 2011, 2012; Murray 2011; Ostriker & Shetty 2011; Zhang & Thompson 2012). However, the integrated mass and momentum in these outflows, their detailed density and velocity statistics, and the lifetime star-forming efficiency and destruction timescale of GMCs all depend strongly on how radiation interacts with the highly turbulent and inhomogeneous gas and dust within these clouds.

One of the hallmarks of GMC structure is the clumpy, filamentary morphology produced by the interaction between gravitational collapse and turbulence (e.g., McKee & Ostriker 2007; André et al. 2014). The initially turbulent cloud is characterized by a lognormal column density probability density function (PDF) (Ostriker et al. 2001; Vázquez-Semadeni & García 2001; Padoan et al. 2004a, 2004b; Goodman et al. 2009; Kainulainen et al. 2009; Brunt et al. 2010; Lombardi et al. 2010;

Price et al. 2011; Schneider et al. 2013, 2015; Butler et al. 2014; Lim et al. 2016), with most of the mass concentrated well above the mean (area-weighted) cloud surface density. Gravitational collapse further enhances this contrast, and the PDF may develop a power-law tail at the high column densities associated with star-forming cores (Klessen et al. 2000; Federrath et al. 2008; Vázquez-Semadeni et al. 2008; Ballesteros-Paredes et al. 2011; Kritsuk et al. 2011; Collins et al. 2012; Federrath & Klessen 2013; Lee et al. 2015; Lombardi et al. 2015). It is therefore clearly necessary to understand how radiation from dispersed stellar sources is filtered through such a top-heavy density PDF in order to understand radiation-driven outflows.

Simultaneously capturing the gravito-turbulent density structure while accurately modeling momentum injection and outflows driven by star formation feedback is very much a work in progress. Instead, almost all semianalytic studies and many numerical ones explicitly (or implicitly) assume spherical symmetry (Matzner 2002; Krumholz & Matzner 2009; Murray et al. 2010; Murray 2011; Dekel & Krumholz 2013; Sales et al. 2014; Kim et al. 2016), so that the evolution is set by the ratio of total momentum injection to gravity. When both radiation and gravity are produced by a central point source, their relative strength may be captured through an average Eddington factor,  $f_{\text{Edd}}$ . Under spherical symmetry, once a shell becomes super-Eddington, i.e.,  $f_{\text{Edd}} \gtrsim 1$ , it can be driven outward to asymptotic velocities exceeding the escape speed of the star-forming region. Murray et al. (2010), Murray (2011) and Thompson et al. (2015) have argued that  $\sim 10^4$  K gas, which is often seen emerging from starburst galaxies at velocities between tens and hundreds of kilometers per second (Heckman et al. 1990; Steidel et al. 1996; Franx et al. 1997; Pettini et al. 2000, 2001; Shapley et al. 2003; Martin 2005;

Rupke et al. 2005; Tremonti et al. 2007; Weiner et al. 2009; Ménard et al. 2011), may have been accelerated by radiation forces from massive central star clusters. However, it remains unclear which theoretical results based on spherical symmetry carry over and which must be strongly modified when the filamentary gas structure is taken into account. Murray et al. (2010), Hopkins et al. (2011), and Thompson & Krumholz (2016) considered parameterizations of the column density PDF as a lognormal distribution, with the first two studies concluding that the mean radiation force would not differ substantially from the case of a uniform gas distribution, and the last pointing out that some lines of sight could be super-Eddington (enabling wind driving) even if the average conditions are sub-Eddington. Because the variance in the lognormal increases with turbulent Mach number, the radiation-matter coupling is expected to be much more affected by inhomogeneity in the cold ISM phase than in the warm ISM phase, and this could also have implications for driving cold versus warm galactic winds.

Numerical simulations of turbulent self-gravitating clouds have tended to concentrate on the dynamics of expanding H II regions driven by ionized gas pressure, which has generally been found to be inefficient at producing outflows and dispersing clouds (Dale et al. 2005, 2012, 2013; Vázquez-Semadeni et al. 2010; Walch et al. 2012; Colín et al. 2013). A series of simulations by Dale et al. (2005, 2012, 2013) found that filamentary structure reduces the fraction of gas that is ionized to a small portion of the cloud mass, with ionized gas escaping to low-density regions. As shown by these studies, pressure from photoionized gas was capable of expelling substantial material only when the escape speed was lower than the ionized gas sound speed ( $\sim 10 \text{ km s}^{-1}$ ).

Overall, radiation forces from the non-ionizing component are expected to dominate ionized gas pressure in clouds with high surface density and cloud mass (Fall et al. 2010; Kim et al. 2016), and there is some observational support for this (Pellegrini et al. 2007, 2010; Lopez et al. 2011, 2014). Over the lifetime of a star cluster, the influence of radiation pressure will still be significantly lower than that of supernovae (SNe) II (Elmegreen & Scalo 2004; Mac Low & Klessen 2004), which inject an order of magnitude more momentum to the ISM overall (Ostriker & Shetty 2011; see also Kim & Ostriker 2015; Iffrig & Hennebelle 2015; Walch & Naab 2015; Martizzi et al. 2015 for assessments of momentum injection by SNe). However, the delay of SNe by 3–30 Myr means that the filamentary environment into which they deposit their energy will likely already have been shaped by other forms of feedback. Walch & Naab (2015) find that clouds that have previously been photoionized absorb 50% more SN energy and are more likely to be disrupted. Meanwhile, Iffrig & Hennebelle (2015) found that supernovae exploding near the edge of a cloud have a weaker impact overall, especially on transferring momentum to the dense gas, than fully embedded supernovae; this again suggests that preprocessing of GMCs by radiation will be important to the subsequent interaction with supernova blast waves. Thus, the significant radiation pressure present in massive clouds and clusters may play as crucial a role in the dispersal of GMCs, even though supernovae are intrinsically more powerful.

To date, only a few simulations have addressed the effect of either direct or reprocessed radiation on turbulent molecular gas via fully self-consistent radiation hydrodynamic (RHD)

simulations (Krumholz & Thompson 2012, 2013; Davis et al. 2014; Skinner & Ostriker 2015; Raskutti et al. 2016). These have generally found that momentum deposition is less efficient in a turbulent filamentary medium than for the case of a uniform spherically symmetric shell. For plane-parallel simulations of IR radiation interacting with gas using opacity  $\kappa \propto T^2$  with a fixed external gravitational potential and fixed total flux (Krumholz & Thompson 2012; Davis et al. 2014), the measured radiation force was reduced by some tens of percent up to a factor  $\sim 2$  through the anticorrelation of matter and radiation in a turbulent medium. The simulations of Skinner & Ostriker (2015), with fixed opacity, and including self-gravity from both gas and the star particles that form over time, found similar reductions in the radiation force as a result of matter/radiation anticorrelations.

This is the third paper of a series in which we apply the *Hyperion* RHD code (Skinner & Ostriker 2013) to consider evolution of self-gravitating turbulent clouds in response to the radiation formed by stars in collapsed regions. Skinner & Ostriker (2015) considered the regime of massive clouds that are optically thick to reprocessed radiation. Their work showed that reprocessed radiation only expels mass when the Eddington ratio for IR radiation,  $f_{\text{Edd},*} \equiv \kappa_{\text{IR}} \Psi / (4\pi Gc)$ , exceeds unity, where  $\kappa_{\text{IR}}$  is the mean IR opacity and  $\Psi$  the mean light-to-mass ratio of stars. However, even for cases with  $f_{\text{Edd},*} > 1$ , the net star-forming efficiency does not follow the scaling prediction ( $\epsilon_{\text{final}} \propto \kappa_{\text{IR}}^{-1}$ ) from simple spherical shell models because radiation and matter tend to be more anticorrelated at higher  $\kappa_{\text{IR}}$ . For clouds destroyed by radiation, the mean velocity of ejected gas is  $\sim 1$ –2 times the cloud’s escape speed at its surface.

Raskutti et al. (2016, hereafter Paper I) applied the *Hyperion* code in the opposite single-scattering limit to clouds with a wide range of masses and sizes. These simulations showed that star formation continues unabated past the point that the radiation force becomes super-Eddington based on a cloud’s mean global properties (i.e., in the spherical idealization). This is because the Eddington ratio for a given structure is inversely proportional to its column density, and the lognormal distribution of column densities in a cloud implies that most of the gas mass is at column densities higher than the volume-weighted mean. As a consequence, the net star-forming efficiency required for radiation forces to disperse the remaining gas can be an order of magnitude higher than would be expected based on a spherically symmetric idealization. We showed that the net star-forming efficiency in simulated clouds can be predicted accurately, given knowledge of the mean and variance of the cloud’s column density PDF. The net star formation efficiency (SFE) found in Paper I can be considered an upper limit, since the only process that prevented star formation was feedback by non-ionizing far-ultraviolet (FUV). In reality, other internal feedback processes, as well as external dynamical effects, may disperse the material in a star-forming cloud before this “FUV feedback-limited-efficiency” is reached.

Here, we consider the simulations presented in Paper I in further detail. We seek to understand how radiation feedback alters the structure of stars and gas initially established by gravity and turbulence, and how this distribution then sets the cloud disruption times, the overall momentum input to the gas, and the statistics of velocities in the outflowing gas. As in Paper I, we emphasize that our simulations, like other current numerical simulations, are not comprehensive models of star-forming clouds. Rather, they should be considered controlled numerical

experiments that are designed to focus on a particular process (here, the dynamical interaction between FUV radiation and cold, turbulent, self-gravitating gas), and to systematically analyze it under a range of parameterized conditions (here, principally, cloud mass and size).

Other forms of feedback (ionizing radiation, stellar winds, and supernovae from high-mass stars; prestellar outflows from low-mass stars) that we do not include would contribute to stirring up turbulence and driving outflows that could unbind cluster-forming clumps and clouds, and some of these may be more dynamically important than FUV radiation forces. In addition, other idealizations that we adopt (such as not including thermal feedback, and omitting magnetic fields) may quantitatively affect the results, even if FUV radiation forces were to dominate other dynamical feedback. Furthermore, realistic GMCs are never isolated, but are subject to larger-scale galactic processes (including nearby supernovae) that may act to disperse a cloud on a shorter timescale than internal feedback is able to be effective.

Nevertheless, focused simulations and analyses of the kind we present here provide essential physical insight, and represent an important step toward future simulations that are more comprehensive and therefore better models of real astronomical systems. In the present case, because the models of Paper I and those we describe here are the first direct numerical RHD simulations investigating the effects of FUV radiation pressure feedback in turbulent clouds, we believe it is valuable to analyze this process in detail before adding other physics.

We begin in Section 2 by describing the *Hyperion* code and the numerical setup of our turbulent clouds. In Section 3 we present an overview of the time evolution for a number of models. In Section 4 we analyze the overall profiles of gas, stars, radiation, and the Eddington force ratio in our simulations. Section 5 quantifies the statistical distributions of gas surface density, which govern the interaction between matter and radiation; we also measure the absorption fraction of radiation and the total momentum imparted to the gas at different stages of evolution. Section 6 analyzes the velocity statistics of material streaming away from the central star clusters and provides a simple interpretation based on radiative acceleration of a lognormal surface density distribution. Finally, we summarize and discuss our conclusions in the context of other theoretical work and observations in Section 7.

## 2. Numerical Setup

### 2.1. Equations and Algorithms

We run three-dimensional RHD simulations on a Cartesian grid using the *Hyperion* (Skinner & Ostriker 2013) extension to the *Athena* code (Stone et al. 2008). We refer to Skinner & Ostriker (2013) for a more detailed description of the *Hyperion* code and to Paper I for details concerning the implementation of our simulations. However, we give a brief overview here.

As we are operating in the single-scattering limit, we can ignore radiative thermal emission terms, and the simplified mixed-frame equations of RHD become

$$\partial_t \rho + \nabla \cdot (\rho \mathbf{v}) = 0, \quad (1)$$

$$\partial_t (\rho \mathbf{v}) + \nabla \cdot (\rho \mathbf{v} \mathbf{v} + P \mathbb{I}) = -\rho \nabla \Phi + \rho \kappa \frac{\mathbf{F}}{c}, \quad (2)$$

$$\frac{1}{\hat{c}} \partial_t \mathcal{E} + \nabla \cdot \left( \frac{\mathbf{F}}{c} \right) = -\rho \kappa \mathcal{E} + \mathbb{S}, \quad (3)$$

$$\frac{1}{\hat{c}} \partial_t \left( \frac{\mathbf{F}}{c} \right) + \nabla \cdot \mathbb{P} = -\rho \kappa \frac{\mathbf{F}}{c}, \quad (4)$$

where  $\rho$ ,  $\mathbf{v}$ , and  $P$  are the gas density, velocity, and pressure, and  $\Phi$  is the gravitational potential, all evaluated in the laboratory frame. The variables  $\mathcal{E}$ ,  $\mathbf{F}$ , and  $\mathbb{P}$  are the radiation energy density, flux vector, and pressure tensor, respectively, again evaluated in the laboratory frame, while  $\kappa$  is the frequency-weighted specific material opacity calculated in the gas rest frame. This opacity is set to  $\kappa = 1000 \text{ cm}^2 \text{ g}^{-1}$ , consistent with the radiation pressure cross sections per H derived from the Weingartner & Draine (2001) dust model (Draine 2011). We note that Equations (3) and (4) are respectively obtained as the zeroth and first moments of the equation of radiative transfer for monochromatic radiation.

Our simulations adopt the simplifying assumption of an isothermal equation of state for the gas, with  $P = c_s^2 \rho$  and  $c_s = 0.2 \text{ km s}^{-1}$ , corresponding to a gas temperature of  $T \sim 10 \text{ K}$ . Temperatures similar to this (or slightly higher, up to 50 K) are characteristic of most of the mass in observed GMCs (e.g., Scoville & Solomon 1975; Scoville et al. 1987; Roman-Duval et al. 2010; Heyer & Dame 2015), and are consistent with the balance between typical galactic heating rates (by either cosmic rays or the photoelectric effect) and line cooling in molecular gas. In adopting an isothermal assumption at a temperature consistent with cosmic-ray heating, we ignore heating by both ionizing and non-ionizing radiation, which would affect the gas exposed to unattenuated radiation from the young stars embedded in the clouds. As dust shielding limits the effects of non-ionizing radiative heating to either low-density material or to the cores surrounding young stars, we assume that this will have negligible impact on most of the gas in both clouds and outflows. Ionizing radiation may create regions of both high temperature and pressure—with significant dynamical consequences—in some parameter regimes; we will address the relative roles of ionizing and non-ionizing radiation in a future publication.

*Hyperion* closes the two radiation moment equations above by adopting the  $M_1$  relation (Levermore 1984). This expresses the pressure tensor in terms of  $\mathcal{E}$  and  $\mathbf{F}$ , with  $\mathbb{P} \rightarrow (1/3)\mathcal{E}\mathbb{I}$  in the diffusion limit ( $|\mathbf{F}|/\mathcal{E} \ll 1$ ) and  $\mathbb{P} \rightarrow \mathcal{E}\hat{\mathbf{n}}\hat{\mathbf{n}}$  in the streaming limit ( $|\mathbf{F}|/\mathcal{E} \rightarrow 1$ ), where  $\hat{\mathbf{n}} = \mathbf{F}/|\mathbf{F}|$ . As the radiation equations are advanced in time via an explicit update, *Hyperion* ensures that the timesteps for radiation field updates are not unfeasibly short by adopting the reduced speed of light approximation (RSLA; Gnedin & Abel 2001). In practice, for radiation in the single-scattering limit, the reduced propagation speed  $\hat{c}$  must satisfy  $\hat{c} \sim 10v_{\text{max}} \gg v_{\text{max}} \sim 25\text{--}50 \text{ km s}^{-1}$  depending on the initial cloud surface density (see Skinner & Ostriker 2013, and Paper I for a detailed discussion of requirements for the RSLA).

Stellar emission is represented by the term  $\mathbb{S}$  in Equation (3). Monochromatic radiation from the star particles is emitted isotropically, representing idealized luminous stellar clusters. The source function  $\mathbb{S} = j_*/c$  for each particle of mass  $M_*$  is Gaussian, with

$$j_*(r) = \frac{L_*}{(2\pi\sigma_*^2)^{3/2}} \exp\left(-\frac{r^2}{2\sigma_*^2}\right), \quad (5)$$

and with (fixed) radius  $r_* = \sqrt{2 \ln 2} \sigma_* = 1$  pc and fixed luminosity per unit mass  $\Psi \equiv L_*/M_*$  typical of young luminous clusters. We adopt a fiducial value of  $\Psi = 2000$  erg s<sup>-1</sup> g<sup>-1</sup> characteristic of a fully sampled Kroupa initial mass function (IMF; Dopita et al. 2006; we again refer to Paper I for a more detailed discussion). We note that the assumption of a constant value for  $\Psi$  is an idealization adopted for simplicity in this first study. In a real cluster, the light-to-mass ratio begins to decline significantly after  $\sim 5$  Myr, whereas many of our simulations have not reached completion (in the sense of either forming stars or driving out most of the initial gas in the cloud) within 5 Myr from the onset of star formation.

A source size  $r_* = 1$  pc is chosen for both physical reasons (this is comparable to radii of observed clusters; e.g., Pfalzner et al. 2016) and numerical reasons (this allows us to resolve source regions with our values of  $\Delta x$ ). We note, however, that with our radiation solver, the radiation force will always be smaller than that of a point source at some scale, here  $r \lesssim 1$  pc. This implies that ongoing accretion onto star particles may be overestimated, even considering just the non-ionizing radiation (ionizing radiation would also create high-pressure non-accreting H II regions near stars, which the present simulations do not capture). Nevertheless, the lack of resolution in the immediate neighborhood of sink particles does not affect the interaction between radiation and gas at larger scales, including driving outflows from star-forming regions, which is the main focus of the present study.

We note that the M1 closure does not allow beams of radiation to cross (instead they merge), and more generally can fail to provide an accurate solution for the radiation field when sources are spatially widely distributed in an optically thin region. For the current study, we are interested in the interaction of the radiation field with the gas on the overall cloud scale, whereas the individual star particles tend to be spatially concentrated. With this source and “screen” geometry, the limitations of the M1 approximation are less likely to affect the solution. To check this, we have compared the solution returned by the M1 solver with the solution computed by an adaptive ray-tracing solver (for identical source and density distribution), and found good agreement, except in the immediate vicinity of sources (Kim et al. 2017).

The star particles themselves are represented within the code by point-mass sink particles (Gong & Ostriker 2013) formed when cells exceed the Larston–Penston (Larson 1969; Penston 1969) density threshold  $\rho_{\text{th}} = 8.86 c_s^2 / (\pi G \Delta x^2)$  and are also local minima of the gravitational potential (Banerjee et al. 2009; Federrath et al. 2010; Vázquez-Semadeni et al. 2011). Star particles are initialized with their mass and momentum equal to that of the gas inside a control volume of width  $3\Delta x$ . They are then evolved forward in time using a leapfrog kick-drift-kick method (Springel 2005), where the particles’ positions and momenta are alternately updated using the particles’ velocities and the total gravitational potential, respectively. The gravitational potential combines that of the stars and gas and is computed via a Fourier method on a domain equivalent to eight times the computational volume in order to implement vacuum boundary conditions for  $\Phi$  (Hockney & Eastwood 1981). The density distribution input to the Poisson solver uses a particle-mesh method with a triangular-shaped cloud kernel to smoothly add each star particle’s mass to the gas density grid (Hockney & Eastwood

1981). Finally, gas is accreted onto the star particles using the HLL flux at the interface between sink control volumes and the rest of the grid, and sink particles are merged when their control volumes overlap.

*Hyperion* solves for the gas and radiation variables by splitting Equations (1)–(4) into separate subsystems to account for the very different timescales involved. The gas subsystem is solved using *Athena*’s unsplit Van Leer (VL) integrator (Stone & Gardiner 2009). The hydrodynamic timestep is determined using a radiation-modified CFL condition with a Courant number of 0.4 (the typical value adopted in VL integration schemes) and a radiation-modified effective sound speed, which accounts for the added effect of radiation pressure in optically thick zones,  $c_{\text{eff}} \equiv \sqrt{(\gamma P + 4/9 \mathcal{E}(1 - e^{-\rho \kappa_0 \Delta x}))} / \rho$  (Krumholz et al. 2007).

In general, *Hyperion* solves the radiation subsystem using a further operator splitting, which separates the radiation source terms into explicit and implicit terms. However, since we consider only radiative absorption and not reemission, source terms can all be solved non-iteratively. In particular, the radiation source term  $\mathcal{S}$  in Equation (3), the flux absorption term  $-\rho \kappa \mathbf{F} / c$  in Equation (4), and the radiation energy absorption term  $-\rho \kappa \mathcal{E}$  in Equation (3) are solved on the radiation timescale using a standard backward Euler update. This radiation timestep is set by a CFL condition based on the radiation signal speed  $\hat{c}$ , so that there are roughly 10 radiation substeps for each update to the gas subsystem.

## 2.2. Initial Conditions

We consider the same set of self-gravitating star-forming clouds as described in Paper I, evolved for about four initial freefall times, so that all of the unaccreted gas is expelled from the simulation volume. All clouds discussed here are evolved at a resolution of  $256^3$  (see Paper I for a description of convergence tests). Each cloud is initialized as a uniform-density sphere, with  $\rho_0 = 3M_{\text{cl},0} / (4\pi r_0^3)$ , where  $r_0$  is the initial cloud radius. The clouds are centered inside cubic simulation volumes of length  $L = 4r_0$  with outflow boundary conditions in order to track both the mass and momentum expelled at relatively large radius. The gas surrounding the cloud is initialized at a factor of  $10^3$  lower than the cloud density, so that the total mass on the grid outside the cloud is  $\sim 0.015 M_{\text{cl},0}$ .

Both inside and outside the cloud, the grid is initialized with a turbulent velocity field as described in Stone et al. (1998), Skinner & Ostriker (2015) and Paper I. This field is generated as a Gaussian random field in Fourier space such that over the range  $k \in [2, 64] \times 2\pi/L$ ,  $\delta v_k$  is chosen from a Gaussian distribution with variance  $P(k) \propto k^{-4}$ , consistent with observed GMCs (e.g., Dobbs et al. 2013). The velocity field is then transformed back to real space and renormalized in terms of the virial parameter  $\alpha_{\text{vir},0} \equiv 2E_K / |E_G|$ , so that the initial variance of the velocity distribution is  $v_{\text{rms}}^2 = 2E_K / M_{\text{cl},0} = \alpha_{\text{vir},0} E_G / M_{\text{cl},0}$ , where  $E_K$  is the total initial turbulent gas kinetic energy and  $E_G = -3GM_{\text{cl},0}^2 / (5r_0)$  is the cloud’s initial gravitational binding energy. Finally, the momentum field is forced to have zero mean by subtracting off the initial net momentum of the cloud. We note that this procedure results in roughly a 2:1 ratio of energy in solenoidal and compressive modes, respectively.

In Table 1 we list simulation inputs for our fiducial model, including the initial cloud mass, radius, and virial parameter, and the parameters  $c_s$ ,  $\hat{c}$ ,  $\Psi$  and  $\kappa$ . In Table 2 we show simulation parameters and results for all models we discuss. Note that in our model nomenclature,  $\Sigma$ -M5E4-R15 designates

**Table 1**  
Fiducial Parameters

Parameter	Value
$\alpha_{\text{vir},0}$	2.0
$r_0$	15 pc
$M_{\text{cl},0}$	$5 \times 10^4 M_{\odot}$
$\Sigma_{\text{cl},0}$	$70.74 M_{\odot} \text{ pc}^{-2}$
$t_{\text{ff}}$	4.29 Myr
$v_{\text{rms}}$	$4.16 \text{ km s}^{-1}$
$v_{\text{esc}}$	$5.36 \text{ km s}^{-1}$
$c_s$	$0.2 \text{ km s}^{-1}$
$\hat{c}$	$250 \text{ km s}^{-1}$
$\Psi$	$2000 \text{ erg s}^{-1} \text{ g}^{-1}$
$\kappa$	$1000 \text{ cm}^2 \text{ g}^{-1}$

the model with initial mass  $5 \times 10^4 M_{\odot}$  and radius 15 pc. For reference, note that Table 2 in Paper I also provides initial density, freefall time, initial turbulent velocity dispersion, and initial escape speed for each of these models. All of the models considered here have as initial virial parameter  $\alpha_{\text{vir},0} = 2$ , which represents a marginally gravitationally bound state. For several of our analyses, we focus on a subset of three simulations extracted from these models. We consider our fiducial model, Run I, as well as low- and high surface density models with  $M = 2 \times 10^4 M_{\odot}$ ,  $R = 15$  pc (model  $\Sigma$ -M2E4-R15); and  $M = 2 \times 10^5 M_{\odot}$ ,  $R = 15$  pc (model  $\Sigma$ -M2E5-R15)—Run II and Run III, respectively—shown in italics in Table 2. For each of these models, we also consider the case in which no radiative feedback is included (Runs Ia, IIa, and IIIa).

Table 2 shows that the initial freefall time varies from  $t_{\text{ff}} = 1.31$  Myr in our highest-density model to  $t_{\text{ff}} = 15.3$  Myr in our lowest-density model. As discussed in Paper I, evolutionary times in our simulations tend to scale with the respective value of  $t_{\text{ff}}$ . For example, the onset time of star formation  $t_*$  varies across the suite of models by just 20% upward and downward from  $t_*/t_{\text{ff}} = 0.5$ , whereas the physical onset time varies from  $t_* = 0.5$ –9.8 Myr. In Paper I and here, we therefore generally report times for a given simulation in units of  $t_{\text{ff}}$  for that model. To provide a sense of the corresponding physical times, we also provide various time-scales in Myr for the fiducial simulation.

As in Paper I, we use the notation  $t_x$  to represent the time when approximately  $x\%$  of the final stellar mass has formed. Here, we also use the notation  $t_{\text{of},x}$  to refer to the time when  $x\%$  of the outflowing gas mass has left the simulation volume.

### 3. Overview of Time Evolution—Gas and Radiation Structure

We begin by considering the time evolution of the fiducial model Run I (as described in Section 2). In Figure 1 we show density maps for Run I, viewed both as slices through the stellar center of mass and as Hammer projections of spherical slices around the same center and at various radii. We show slices, with contours of radiation energy density overplotted, at times  $t_2 = 0.44t_{\text{ff}} = 1.9$  Myr (left) and  $t_{50} = 1.04t_{\text{ff}} = 4.5$  Myr (right).

At the earlier time ( $t_2/t_{\text{ff}} = 0.44$ ), the fiducial cloud has already collapsed, with mass gathered by turbulence and self-gravity preferentially along two perpendicular filaments,

although reasonably dense material still extends out to several pc surrounding these filaments. The Hammer projections show evidence of the filamentary nature of the cloud and of an overdensity where a nearby star is forming, but there are relatively few holes in the cloud inside of the original cloud radius (15 pc).

However, by the time half the stars have formed ( $t_{50}/t_{\text{ff}} = 1.04$ ), the structure looks quite different. Radiative feedback has pushed the surrounding gas into much thinner, denser filaments, such that very little of the sky is covered by absorbing gas. Thus, the majority of radiation may freely stream away from sources without imparting momentum to a significant fraction of the gas mass. We note that the structure seen here is quite different from the structure seen in Skinner & Ostriker (2015), where only diffuse IR radiation is included. In that case, the lower opacity for IR compared to UV means that radiation forces are more distributed within the gas (creating less intense compression of filaments) and low-density regions are not as rapidly cleared.

Although the dominant characteristic of cloud structure is the filamentary morphology, clouds also become radially stratified, as we discuss in Section 4 below. Because there is no reemission or scattering of absorbed radiation, the flux is strongly anticorrelated with the circumstellar surface density; this is also evident in the anticorrelation of radiation energy density with gas density. Furthermore, since the dense filaments cover very little solid angle, they are ineffective in shielding low-density gas at large distance from the center, so this gas is rapidly cleared by radiation forces.

All of our simulation runs have the same initial spatial distribution from the initial turbulent velocity field and differ only in the amplitude  $v_{\text{turb}}$ , so that qualitatively similar gas structures and time evolution are evident in both the low- $\Sigma$  and high- $\Sigma$  models (Run II and Run III) compared to the fiducial model (Run I). In the low- $\Sigma$  run, radiation is very efficient at dispersing cloud material and only  $\sim 10\%$  of the initial cloud is converted into stars; the high- $\Sigma$  run has a much higher final SFE  $\sim 60\%$ . In all cases, the tenuous material between filaments is expelled first, and as a consequence, much of the radiation escapes through large holes in the cloud, even in the high- $\Sigma$  model.

### 4. The Profiles of Gas, Stars, and Radiation in the Cloud

As discussed, the morphology of our simulated clouds is highly filamentary, with star formation concentrated in the filaments. Nevertheless, a number of key insights can be gained by considering the angle-averaged profiles of the cloud in spherical shells. Most galaxy formation simulations still struggle to resolve GMC scales, and in some cases (e.g., Olsen et al. 2016) where chemistry and emission properties are of interest, clouds are instead modeled via a sub-grid prescription with an adopted spherical density profile. Meanwhile, numerical or semianalytic models that combine the effects of different types of feedback (e.g., Sales et al. 2014) often rely on assumptions of spherical symmetry for star-forming clouds. As results in these and other applications can depend strongly on the assumed cloud density profile, knowledge of the angle-averaged spherical structure established by turbulence and feedback is desirable.

The radial distribution of gas and stars in our simulations is also interesting because the boundedness and eventual mass distribution of observed stellar clusters depends strongly on how centrally

**Table 2**  
Model Parameters and Results

Model	$\Sigma_{\text{cl},0}$ ( $M_{\odot} \text{ pc}^{-2}$ )	$t_{\text{ff}}$ (Myr)	$t_{50}$ ( $t_{\text{ff}}$ )	$t_{90}$ ( $t_{\text{ff}}$ )	$\alpha$	$f_{\text{unb}}$	$f_{\text{Edd}}$	$\sigma_{\text{in}\Sigma}$	$x$	$f_{\text{abs}}$	$\frac{\langle p_{r,\text{tot}} \rangle}{p_{*}}$	$\frac{\langle p_r \rangle}{M_{*}}$ ( $\text{km s}^{-1}$ )
$\Sigma$ -M2E4-R25	10.13	14.6	0.88	1.51	0.84	0.27	64.58	$1.55^{+1.23}_{-0.33}$	$1.49^{+0.69}_{-0.27}$	0.37	0.84	38.28
$\Sigma$ -M5E4-R35	12.92	15.3	1.07	2.05	1.16	0.59	10.24	$1.64^{+0.23}_{-0.47}$	$1.62^{+1.75}_{-0.45}$	0.39	1.44	31.79
$\Sigma$ -M2E4-R20	15.83	10.5	1.08	1.73	1.00	0.22	127.16	$1.60^{+0.27}_{-0.42}$	$1.61^{+0.08}_{-0.42}$	0.44	0.78	20.64
$\Sigma$ -M5E4-R25	25.33	9.24	1.01	1.71	0.92	0.25	9.82	$1.44^{+0.01}_{-0.27}$	$1.36^{+0.37}_{-0.20}$	0.50	1.12	25.72
$\Sigma$ -M1E5-R35	25.84	10.8	1.00	1.53	1.20	0.19	9.85	$1.51^{+0.02}_{-0.34}$	$1.41^{+0.23}_{-0.25}$	0.62	2.06	35.39
<i><math>\Sigma</math>-M2E4-R15</i>	<i>28.14</i>	<i>6.79</i>	<i>1.07</i>	<i>1.65</i>	<i>1.00</i>	<i>0.14</i>	<i>8.65</i>	$1.38^{+0.05}_{-0.16}$	$1.36^{+0.23}_{-0.18}$	<i>0.53</i>	<i>0.76</i>	<i>15.02</i>
$\Sigma$ -M1E4-R10	31.66	5.23	1.09	1.64	1.05	0.11	39.70	$1.55^{+0.10}_{-0.31}$	$1.49^{+0.26}_{-0.29}$	0.45	0.42	12.92
$\Sigma$ -M5E4-R20	39.57	6.61	1.02	1.51	1.16	0.01	9.33	$1.36^{+0.04}_{-0.18}$	$1.28^{+0.28}_{-0.12}$	0.65	0.94	22.30
$\Sigma$ -M1E4-R08	49.46	3.74	1.11	1.75	1.02	0.44	37.57	$1.52^{+0.15}_{-0.24}$	$1.43^{+0.70}_{-0.22}$	0.45	0.35	9.25
$\Sigma$ -M1E5-R25	50.65	6.54	1.05	1.48	1.14	0.01	8.68	$1.36^{+0.06}_{-0.19}$	$1.27^{+0.18}_{-0.11}$	0.66	1.06	26.50
$\Sigma$ -M2E5-R35	51.69	7.66	1.08	1.51	1.28	0.10	7.28	$1.45^{+0.02}_{-0.27}$	$1.34^{+0.26}_{-0.18}$	0.70	1.66	34.43
$\Sigma$ -M5E3-R05	63.31	2.61	1.17	1.95	0.91	0.05	34.53	$1.65^{+0.10}_{-0.33}$	$1.59^{+0.91}_{-0.35}$	0.27	0.28	6.41
$\Sigma$ -M2E4-R10	63.31	3.70	1.21	1.83	0.86	0.02	6.19	$1.72^{+0.14}_{-0.20}$	$1.61^{+0.54}_{-0.24}$	0.49	0.40	10.70
<b><math>\Sigma</math>-M5E4-R15</b>	<b>70.35</b>	<b>4.29</b>	<b>1.06</b>	<b>1.57</b>	<b>1.16</b>	<b>0.03</b>	<b>13.21</b>	$1.39^{+0.05}_{-0.24}$	$1.27^{+0.37}_{-0.13}$	<b>0.61</b>	<b>0.60</b>	<b>16.41</b>
$\Sigma$ -M1E5-R20	79.14	4.67	1.02	1.56	1.13	0.03	4.30	$1.41^{+0.02}_{-0.29}$	$1.27^{+0.32}_{-0.14}$	0.70	0.95	21.14
$\Sigma$ -M2E4-R08	98.93	2.64	1.10	1.71	1.09	0.02	7.49	$1.44^{+0.11}_{-0.21}$	$1.32^{+0.39}_{-0.15}$	0.44	0.31	8.50
$\Sigma$ -M2E5-R25	101.30	4.62	1.04	1.57	1.17	0.02	4.70	$1.43^{+0.05}_{-0.33}$	$1.28^{+0.31}_{-0.17}$	0.76	1.17	28.09
$\Sigma$ -M1E4-R05	126.63	1.85	1.16	1.80	1.14	0.02	5.71	$1.55^{+0.04}_{-0.26}$	$1.42^{+0.35}_{-0.21}$	0.23	0.22	5.93
$\Sigma$ -M1E5-R15	140.70	3.04	1.04	1.63	1.10	0.03	4.75	$1.36^{+0.14}_{-0.25}$	$1.24^{+0.45}_{-0.12}$	0.68	0.50	16.49
$\Sigma$ -M5E4-R10	158.29	2.34	1.09	1.67	1.12	0.04	4.19	$1.39^{+0.08}_{-0.24}$	$1.27^{+0.33}_{-0.13}$	0.55	0.34	9.93
$\Sigma$ -M2E5-R20	158.29	3.31	1.09	1.65	1.12	0.01	4.19	$1.31^{+0.07}_{-0.21}$	$1.21^{+0.34}_{-0.10}$	0.77	0.64	19.96
$\Sigma$ -M5E4-R08	247.32	1.67	1.11	1.77	1.13	0.03	4.49	$1.37^{+0.11}_{-0.23}$	$1.27^{+0.32}_{-0.14}$	0.44	0.30	9.30
$\Sigma$ -M2E4-R05	253.26	1.31	1.20	1.86	1.09	0.01	4.31	$1.48^{+0.12}_{-0.30}$	$1.35^{+0.29}_{-0.21}$	0.20	0.18	6.36
<i><math>\Sigma</math>-M2E5-R15</i>	<i>281.40</i>	<i>2.15</i>	<i>1.22</i>	<i>2.01</i>	<i>0.91</i>	<i>0.00</i>	<i>3.31</i>	$1.37^{+0.24}_{-0.21}$	$1.28^{+0.46}_{-0.10}$	<i>0.73</i>	<i>0.37</i>	<i>15.73</i>

**Note.** Columns display the following information: (i) model name, (ii) initial cloud surface density, (iii) initial freefall time, (iv) time  $t_{50}$  when 50% of the star formation is complete, (v) time  $t_{90}$  when 90% of the star formation is complete, (vi) power-law exponent of the fitted density profile at  $t_{50}$  (vii) fraction of the stellar mass that is unbound at the end of the simulation, (viii) Eddington factor, defined in Equation (6), at  $t_{90}$ , (ix) width of the lognormal circumcluster surface density distribution at  $t_{50}$  with error bars given at  $t_{10}$  and  $t_{90}$ , respectively, (x) cloud size factor  $x$ , defined in Equation (8) at the same times as for  $\sigma_{\text{in}\Sigma}$ , (xi) radiation absorption fraction measured 3 Myr after star formation begins, (xii) total radial gas momentum in the simulation volume plus outflowing divided by input stellar radiation momentum, measured 3 Myr after star formation begins, and (xiii) final outflowing gas momentum per unit of stellar mass formed. The fiducial model (Run I) is shown in bold ( $\Sigma$ -M5E4-R15), while the low and high surface density models (Runs II and III) are shown in italics ( $\Sigma$ -M2E4-R15 and  $\Sigma$ -M2E5-R15).

concentrated embedded clusters are within GMCs. Observations suggest that almost  $\sim 90\%$  of all stars formed in molecular clouds are eventually unbound (Lada & Lada 2003), while simulations indicate that the bound fraction depends sensitively on the relative shape of the gas and stellar potentials prior to gas expulsion by feedback (Lada et al. 1984; Goodwin 1997; Adams 2000; Geyer & Burkert 2001; Boily & Kroupa 2003; Goodwin & Bastian 2006; Baumgardt & Kroupa 2007; Proszkow & Adams 2009). In particular, if clusters are more centrally concentrated with a high local SFE, the eventual feedback-driven gas expulsion from large radii will have a limited effect on unbinding the clusters at small radii (see, e.g., Longmore et al. 2014, for a detailed discussion).

#### 4.1. Gas Profiles

In describing radial profiles of the cloud, we choose as our coordinate center the center of mass of the system of star particles. We make this choice because we are primarily interested in the interaction of radiation with the gas, and with an (adopted) constant light-to-mass ratio, the center of the luminosity source is this center of mass. After identifying this center, we interpolate from the Cartesian grid onto a grid in  $[r, \theta, \phi]$  space, where the grid points are spaced equally in  $r$ ,  $\phi$ , and  $\cos \theta$ . We then compute angle-averaged radial profiles,

denoted by  $\langle \cdot \rangle$ , averaging over all  $\theta$  and  $\phi$  at a given radius. In Figure 2(a) we show radial profiles of gas mass enclosed in spherical shells at several different times throughout the fiducial cloud's evolution. As before, times are denoted by  $t_x$  when the stellar efficiency ( $\varepsilon$ ) is at  $x\%$ . For the fiducial model, by the time 10% of the final stellar mass has formed ( $t_{10} = 0.56t_{\text{ff}} = 2.4$  Myr), we find that the cloud's mass profile follows a roughly power-law shape, implying that the underlying gas density profile has itself settled into approximately a power law. The shape of the profile does not change significantly until the very end of star formation, when direct radiation pressure drives strong outflows, compressing the remaining gas into a thin shell.

Parameterizing the density profile as a time-varying power law,  $\rho(r) \propto r^{-\alpha}$ , we find that  $\alpha \sim 1.2$  at  $t_{50}$  for the fiducial model. Figure 2(b) shows that similar results hold true over the full range of clouds that we model, with  $\alpha \sim 1$  at  $t_{50}$ . In Table 2, the values of  $t_{50}$  and  $\alpha$  at  $t_{50}$  are listed for all models. We note that  $\alpha \sim 1$  is shallower than the isothermal or Plummer spheres (Plummer 1911; Whitworth & Ward-Thompson 2001) that are often assumed for GMCs (Sales et al. 2014; Olsen et al. 2016) or seen in observations of the central star-forming core of the Orion Nebula Cluster (Da Rio et al. 2014). It is also shallower than the

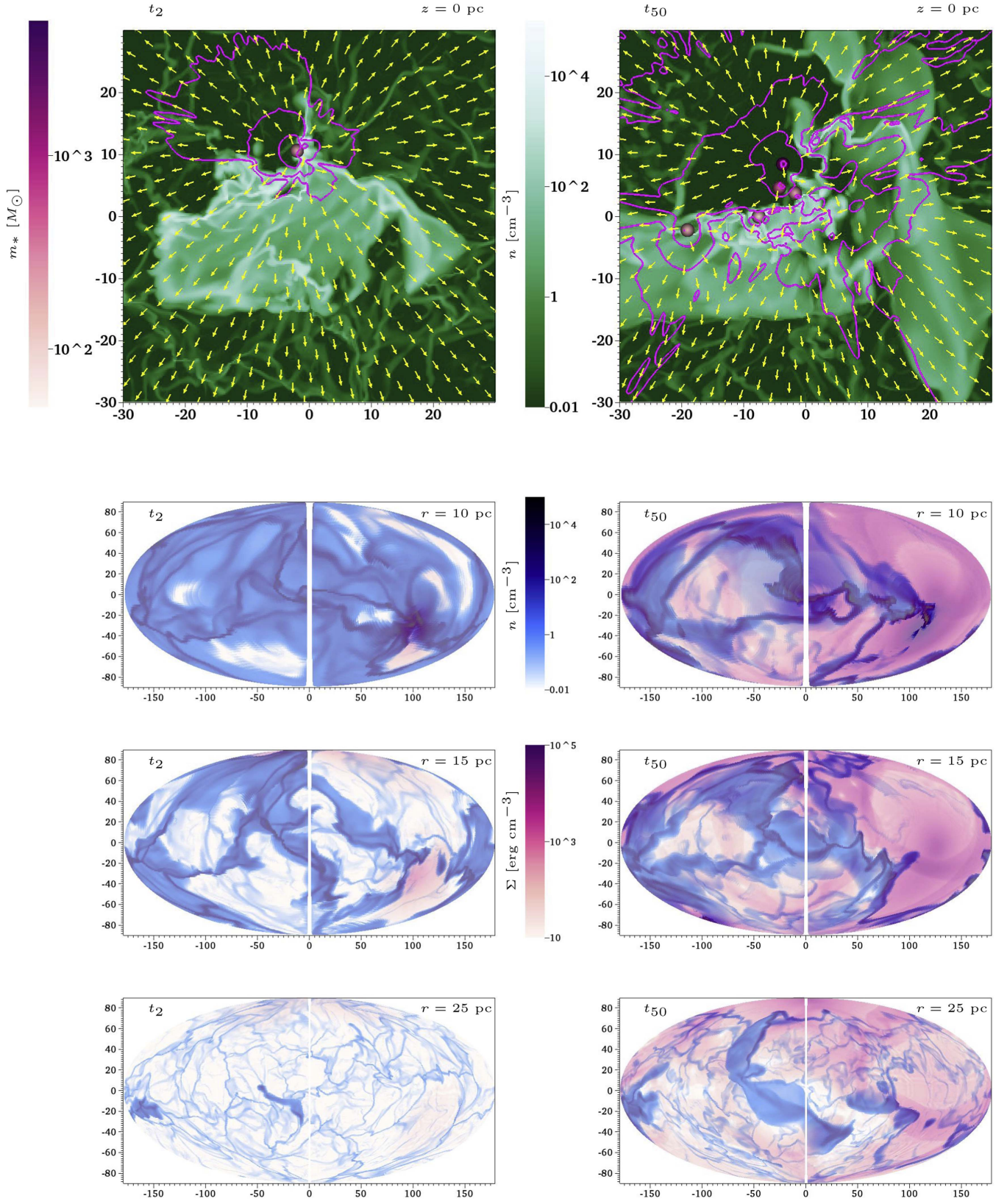


**Figure 1.** Snapshots of the gas density for the fiducial model at times  $t_2/t_{\text{ff}} = 0.44$  (left), and  $t_{50}/t_{\text{ff}} = 1.04$  (right). In physical units, these times are  $t_2 = 1.9$  Myr and  $t_{50} = 4.5$  Myr, when 2% and 50%, respectively, of the final stellar mass in the fiducial model has formed. We show (top) slices through the  $x$ - $y$  plane passing through the position of the stellar center of mass, and (bottom) Hammer projections of spherical slices around that same center, at radii of 10, 15, and 25 pc. In the  $x$ - $y$  slices, the density is shown with a green color scale (in units of  $\text{cm}^{-3}$ , top middle), the directions of radiation flux vectors are overlaid in yellow, and pink contour lines, separated by decades relative to the peak value, show the radiation energy density. Star particles within  $\Delta z = \pm 2$  pc of the slice are plotted as circles, with the color scale for the particle mass (red) in units of  $M_{\odot}$ , shown at the top left. In the Hammer projections, the density is shown with a blue color scale (in units of  $\text{cm}^{-3}$ ), and the radiation energy density is overlaid in pink.

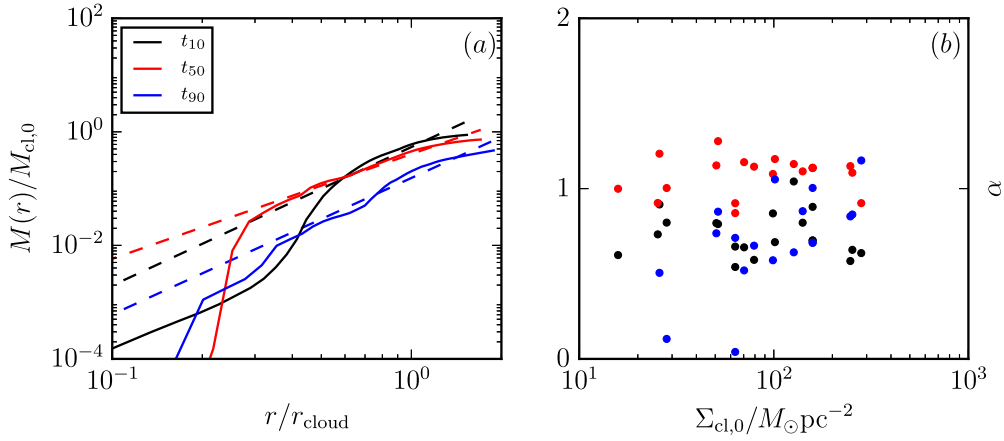


**Figure 2.** Angle-averaged radial profiles of the mass  $M(r) = \int_0^r dr 4\pi r^2 \langle \rho \rangle$  enclosed within a sphere of radius  $r$  (normalized to  $M_{\text{cl},0}$ ) at three different times, denoted by  $t_x$  when the stellar efficiency ( $\varepsilon$ ) is at  $x\%$ . On the left, we show profiles for the fiducial model with radiation feedback, where at each time, we also show the best-fit power law (dashed) over the range between  $r = 3$  and  $15$  pc. On the right, we show best-fit values of the power-law exponent  $\rho(r) \propto r^{-\alpha}$  as a function of initial cloud surface density for all models in the  $\Sigma$ -series.

$\alpha = 1.5$  exponent found in recent simulations (Lee et al. 2015) that do not include feedback. However, we also note that we fit the power law over a large range of radii, and that we lack the resolution necessary to fit the central star-forming region well (in fact, the density profiles do appear steeper in the innermost region).

If we follow the argument of McKee & Tan (2003) that the star formation rate scales with the inverse of the freefall time ( $\sim \rho^{-1/2}$ ) of freely collapsing cores, this would lead to a star formation rate (SFR)  $\propto t^{6/\alpha-3}$ , which would suggest a steep increase in time for  $\alpha \sim 0.8-1.3$ . Instead, as discussed in Paper I, we observe a roughly linear SFR across all surface densities. We believe that this is because the locations (and rate) of collapse are primarily controlled by the filamentary gas structure, and only secondarily by overall cloud stratification.

#### 4.2. Stellar Distribution Profiles

We begin this section by comparing the relative sizes of the nascent stellar clusters and the clouds in which they are embedded. The spatial distribution of star particles has a long tail, since a small number become unbound and escape the simulation volume. We therefore define the size of the cluster as the  $1\sigma$  mass range, i.e., the radius of the sphere about the stellar center of mass containing  $\sim 68\%$  of the stellar mass. Figure 3 compares the evolution in the radius of the stars and gas for Runs I, II, and III, as well as the corresponding Runs Ia, IIa, and IIIa without radiation.

The stellar distributions evolve in very different ways for the three runs. At early times, star formation is far more centrally concentrated in the low surface density Run II, compared to the somewhat larger radial extent in the case of Run III. However, the extended accretion process in Run III binds the cluster more tightly, and the stellar distribution eventually shrinks after  $t \sim t_{\text{ff}}$ . By  $t \sim 1.5t_{\text{ff}}$ , the effective stellar radii of all runs are roughly the same. At late time, the rapid gas expulsion in Run II appears to unbind the cluster as well, its radius increasing secularly in time. For the fiducial model (Run I), the effective stellar radius shrinks after  $t \sim 1.5t_{\text{ff}}$ .

Figure 3 also shows the evolution of stellar distribution in Runs Ia-IIIa, the no-feedback comparison simulations. The most significant difference is that the cluster distribution

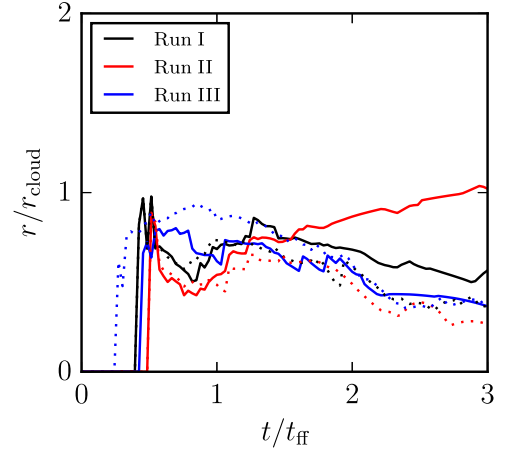


**Figure 3.** Mean size of the stellar mass distributions as a function of time in Runs I-III (solid lines) as well as Runs Ia-IIIa (without feedback, dotted lines). In each case, we show the radius that contains 68% of the mass.

remains bound in Run IIa, the low surface density no-feedback model.

Other low- $\Sigma$  runs show behavior similar to the Run II, with the stellar distribution expanding over time, and a relatively large fraction of the stellar mass unbound at the end of the simulation (see  $f_{\text{unb}}$  in Table 2). Simulations with higher  $\Sigma$  have a very small fraction of the star particles unbound at late times. This suggests that the evolution of the star particle distribution in our simulations is primarily a response to the net SFE in the clouds (which is controlled by radiation pressure feedback), and is low in low- $\Sigma$  clouds and high in high- $\Sigma$  clouds.

Finally, we caution that because of the limited resolution, our star particles do not represent individual stars, so the late-time dynamics may be quite different from that of a real cluster of the same mass.

#### 4.3. Radiation Profiles

We now turn to an exploration of the clouds' internal radiation profiles, focusing on the competition between radiation and gravitational forces. We do this, as before,

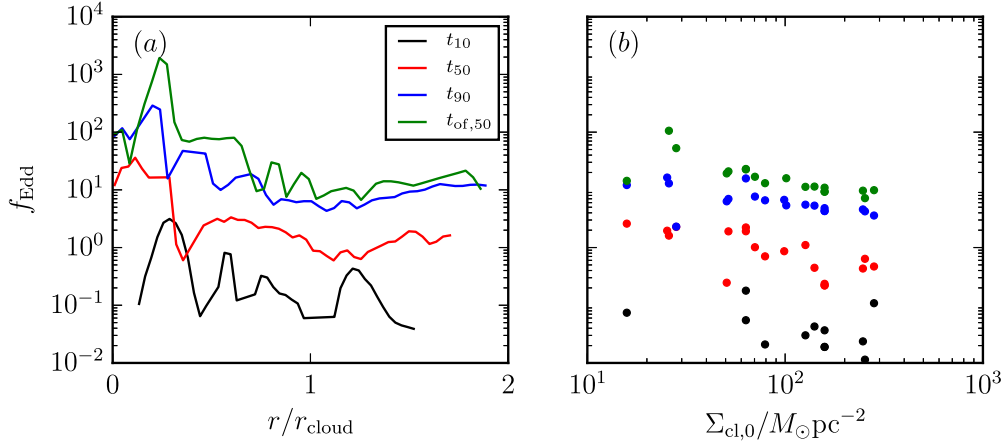


**Figure 4.** Angle-averaged Eddington factor, as described in Equation (6). We show profiles for the fiducial model (left) at four different times when the stellar efficiency or outflow fraction is as shown in the key (see text). For the same respective times in each model, on the right we show the Eddington factor at the cloud radius as a function of initial cloud surface density. We note that particularly at small radii, the Eddington factor may be negative as star particles just exterior to a given shell may dominate the flux. For simplicity, we therefore omit these radii in (a).

using angle-averaged spherical profiles interpolated from the Cartesian grid. The origin of the spherical coordinate grid is at the center of luminosity of the star particle distribution, so that outside of both the stellar and gas distribution (beyond  $\sim 0.8 r_{\text{cloud}}$ ), the angle-averaged flux decreases  $\propto r^{-2}$ .

We may directly compare the influences at different radii of the centrally concentrated radiation sources, and the more distributed gravitational potential, by considering the Eddington factor,  $f_{\text{Edd}}(r)$ . The mean Eddington factor in a given spherical shell is defined as the ratio of the radiation to gravitational forces, given by

$$f_{\text{Edd}}(r) = \frac{\langle \rho \kappa F_r / c \rangle}{\langle \rho \partial_r \Phi \rangle}. \quad (6)$$

For isotropic distributions of gas density and radiation, the force on each fluid element within a given radial shell would be identical. In this case, neglecting hydrodynamic stresses, we would expect star formation to continue until  $f_{\text{Edd}}(r) = \kappa L(r) / [4\pi c GM(r)]$  exceeds unity everywhere in the cloud; here  $L(r)$  and  $M(r)$  are the total luminosity and mass within  $r$ .

Hydrodynamic stresses lead to internal momentum exchange but average to zero over a sufficiently large volume. Thus, it is also interesting to consider the cumulative Eddington factor, defined by

$$f_{\text{Edd,cum}}(r') = \frac{\int_0^{r'} r^2 \langle \rho \kappa F_r / c \rangle dr}{\int_0^{r'} r^2 \langle \rho \partial_r \Phi \rangle dr}, \quad (7)$$

which represents the ratio of the volume-averaged radiation to gravitational forces out to a given radius. In the isotropic case, we might expect star formation to slow when  $f_{\text{Edd,cum}}(r_{\text{cl}}) \sim 1$ . In fact, as discussed in Paper I, the distributions of gas and radiation in the cloud are far from isotropic (or uniform), so that some fluid elements within a given shell may be sub-Eddington even when the angle-averaged Eddington factor exceeds unity. As a consequence, star formation can continue locally even when the mean or cumulative Eddington factor at the cloud radius is well above unity.

Figure 4(a) shows the radial profiles of the angle-averaged Eddington factor  $f_{\text{Edd}}(r)$  for our fiducial model. We show profiles from  $t_{10}/t_{\text{ff}} = 0.56$ ,  $t_{50}/t_{\text{ff}} = 1.06$ ,  $t_{90}/t_{\text{ff}} = 1.57$ , and  $t_{\text{of},50}/t_{\text{ff}} = 2.17$ , where  $t_{\text{of},50} = 9.3$  Myr represents the time when 50% of the mass has been driven out of the cloud by radiation forces.<sup>1</sup>

Since  $r^2 \langle F_r \rangle$  flattens at large radii (because stars are centrally concentrated, and luminosity is attenuated) while  $r^2 \langle \partial_r \Phi \rangle$  continues to increase (from the distributed gas),  $f_{\text{Edd}}(r)$  is expected to be lowest at large radii. Except at the very beginning of star formation, Figure 4 indeed shows that the Eddington factor is largest at small radii and declines outward. Beyond  $\sim 0.5 r_{\text{cl},0}$ , we find that the local and cumulative Eddington factors are approximately equal, particularly at later times, approaching a nearly constant value beyond  $r_{\text{cl},0}$ . Figure 4(b) shows that all of our models reach  $f_{\text{Edd}}(r_{\text{cl},0}) \sim 1$  at  $\sim t_{50}$  when half of their stars are formed, but continue forming stars well beyond this point. By the time star formation is nearly over,  $f_{\text{Edd}}(r_{\text{cl},0})$  is an order of magnitude higher.

We note (see Figure 4(b)) that there is a slight downward trend with initial cloud surface density in the mean Eddington factor at all stages of star formation. In particular, the limiting (i.e., at 90% complete star formation or 50% complete outflow ejection) mean Eddington factor  $f_{\text{Edd}}(r_{\text{cl},0})$  appears to decrease by a factor 5 or more from  $\Sigma \sim 10 M_{\odot} \text{pc}^{-2}$  to  $\Sigma \sim 200 M_{\odot} \text{pc}^{-2}$ . Therefore, there does not seem to be a single, global Eddington factor at which clouds are destroyed. However, we note that in all of our simulations,  $f_{\text{Edd}}(r_{\text{cl},0})$  at this late stage is at least an order of magnitude larger than unity. As we showed in Paper I (see also below), the truncation of star formation by radiation pressure in a turbulent cloud depends on the variance of the surface density distribution, so the range of final  $f_{\text{Edd}}(r_{\text{cl}})$  that we find depends on this variance. The final value of  $f_{\text{Edd}}(r_{\text{cl}})$  would be lower if the surface density variance were lower than it is in our models, which may be true in real clouds.

<sup>1</sup> We note the important caveat that during the later evolutionary stages of the simulation, the timescales are long enough for the radiation field in a real cloud to have declined and for the most massive stars to have exploded as supernovae. The present idealized simulations do not include these effects.

## 5. Statistics of Cloud Structure and Interaction with Radiation

In Section 4.3 we showed that when the angle-averaged Eddington factor reaches a typical value  $\sim 10$  at the cloud radius, star formation shuts down and the remaining gas is ejected from the cloud. This order-of-magnitude increase in  $f_{\text{Edd}}(r_{\text{cl},0})$  (relative to the simple spherically symmetric prediction) mirrors the large increase in the net SFE (compared to the spherical prediction) we found in Paper I. In that work, we argued that the boost in SFE may be attributed to the lognormal distribution of surface densities in the circumcluster gas: high surface density regions remain bound even when the average Eddington factor exceeds unity. Thus, to quench star formation, the luminosity must increase (by forming additional stars) to such a level that even the high- $\Sigma$  tail of the lognormal distribution becomes super-Eddington.

In Paper I, we also showed that the surface density mass PDF (i.e., the distribution of mass as a function of surface density  $\Sigma$  or column densities  $N = \Sigma/\mu$ ),  $P_M(\Sigma)$ , generally has a lognormal shape over the main period of star formation  $t/t_{\text{ff}} \sim 0.5\text{--}1.5$ . Similarly, the surface density area PDF (i.e., the distribution of area as a function of surface density  $\Sigma$ ),  $P_A(\Sigma)$ , also follows a lognormal at the high- $\Sigma$  end, but because the computational domain contains a large low-density volume outside the cloud, there is a low- $\Sigma$  excess above the lognormal from the “non-cloud” material. We showed that  $\sigma_{\ln \Sigma}$  of  $P_M$  and the “cloud” portion of  $P_A$  are the same, as expected. Also as expected, the means are given by  $\langle \ln(\Sigma/\bar{\Sigma}_{\text{cloud}}) \rangle_{M,A} = \pm \sigma_{\ln \Sigma}^2/2$ . In that work, we also showed that while the mean surface density of clouds changes significantly over time as gas is consumed by star formation and ejected by radiation pressure, the value of  $\sigma_{\ln \Sigma}$  evolves much less, and is similar for all of our models.

While in Paper I we analyzed the distribution of surface densities as would be measured in a Cartesian projection by an external observer, the distribution from the point of view of the embedded stars is more relevant when considering the interaction of the gas with radiation. As shown in that work, denoting the current SFE as  $\varepsilon$ , structures with circumcluster surface density  $\Sigma^c$  below  $\Sigma_E = \varepsilon(1 + \varepsilon)^{-1}\Psi(2\pi cG)^{-1}$  will be super-Eddington, hence can be driven out of the cloud, while structures with  $\Sigma^c > \Sigma_E$  cannot. In Paper I, we developed a formalism that provides a prediction for the final SFE in a cloud based on the value for which the largest possible fraction of gas has  $\Sigma^c < \Sigma_E$  and is ejected. We showed that this predicted SFE is in good agreement with the measured final SFEs in our simulations. To provide further quantitative support for the formalism and SFE predictions of Paper I, here we analyze the *circumcluster* surface density distributions for our cloud models.

In addition to determining the fraction of a cloud’s gas mass that is super-Eddington, the circumcluster surface density distributions are also important for determining the fraction of radiation that escapes from the cloud. Finally, since the acceleration of a structure by radiation pressure depends on its surface density, the total momentum and distribution of outflowing gas velocities depend on the distribution of circumcluster surface densities. We start in Section 5.1 by comparing the evolution of observed and circumcluster surface densities, and then in Sections 5.2 and 5.3 provide quantitative measures for their lognormal distributions and for the escape of radiation in all models. In Section 6 we connect the properties

of outflowing gas to the statistics of these circumcluster surface densities.

### 5.1. Evolution of Observed and Circumcluster Surface Density

At any timestep, we can obtain the circumcluster surface density distribution by following the procedure outlined in Section 4. For each point on a grid in  $[r, \theta, \phi]$ , we draw rays from the stellar center of mass to the edge of the box. We then calculate the integral of density along each ray as  $\Sigma^c = \int \rho dr$ . We note that although  $\Sigma^c$  has units of mass/area, it does not correspond exactly to a surface density, except in the special case of a thin shell, since the area of each cell in the  $[r, \theta, \phi]$  grid increases radially outward as  $r^2$ . However, along any given line of sight, if the gas is concentrated over a relatively small radius range,  $\Sigma^c$  represents a local surface density as seen by a central source. For a constant opacity  $\kappa$ , the optical depth along a given ray is  $\Sigma^c \kappa$ .

In the middle row of Figure 5 we show both the “observed” surface density map (projected along  $z$ ) and the Hammer projection of the circumcluster surface density in the fiducial model (Run I) at  $t = 1.57 t_{\text{ff}}$ , when 90% of the final stellar mass has formed. Qualitatively, the maps are quite similar in that gas is concentrated in large dense filaments, which are also the sites of star formation. The top and bottom rows of Figure 5 show corresponding maps for Runs II and III.

However, at this late time, the differential effects of radiative feedback are evident. The most massive star (the farthest east along the equator) and its neighbors have by this stage created a blowout, clearing gas out of the top left corner of the “observed” clouds and a large hole in the east of the Hammer projections. The blowout (and other smaller local bubbles) becomes more pronounced with decreasing surface density (Run I). This reflects the different evolutionary stages of these clouds; the high-density model (Run III) continues to accrete gas onto stars until radiative feedback from the most massive star becomes strong enough to evacuate its local environment.

### 5.2. Gas Density PDF

We are most interested in the shape of the circumcluster surface density distribution and how close this is to the lognormal form of the observed surface density. In Figure 6 we show results from the fiducial model at four times: (a)  $t_{10}$ , (b)  $t_{50}$ , (c)  $t_{90}$ , and (d)  $t_{\text{of},50}$ . At each time, we show the PDF (mass fraction) as functions of both observed surface density and circumcluster surface density. The distributions of circumcluster surface density  $\Sigma_*^c$  are calculated by omitting gas inside the mean stellar radius, since much of the gas near the center of the cloud lies between stars, and hence would see a radiation force from many surrounding star particles, which may cancel out. Therefore, if we are interested in the interaction of gas with radiation forces, the effective surface density distribution of material surrounding the whole ensemble of stars is better characterized by  $\Sigma_*^c$ . For any given circumcluster ray, the mass is computed as  $dM = d\Omega \int_{r_{\text{min}}}^{r_{\text{max}}} \rho r^2 dr$ , where  $d\Omega = d\phi \sin \theta d\theta$  is the solid angle. In each panel we also show best-fit lognormals for each PDF.

At all times, both the observed and circumcluster mass PDFs appear to be quite close to lognormal in shape. The  $\Sigma_*^c$  distributions are quite similar in their mean and variance to that of the “observed”  $\Sigma$  distribution. This suggests that the combination of turbulence and gravity creates a structure so

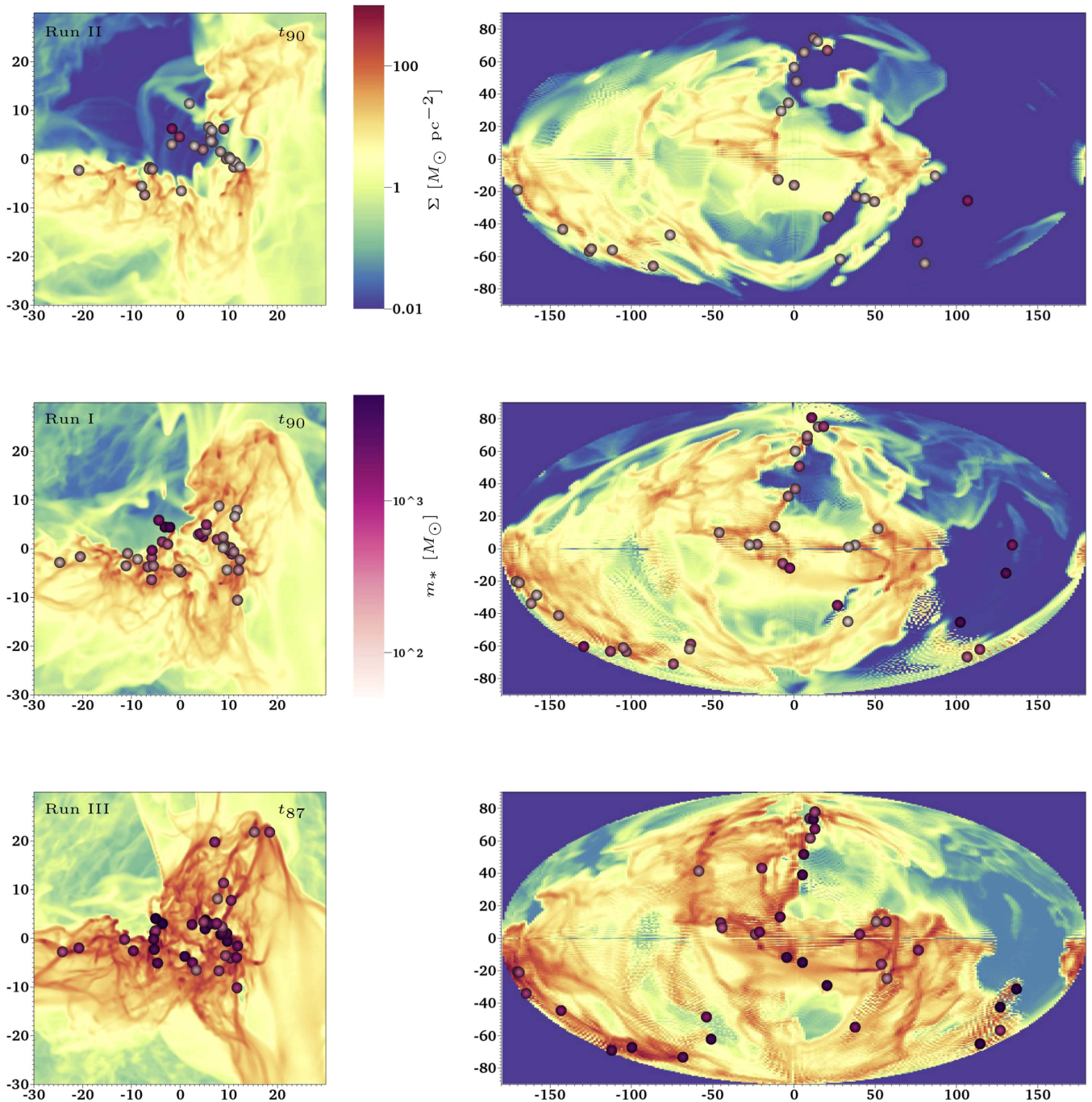


**Figure 5.** Snapshots of the surface density at time  $t = 1.57 t_{\text{ff}} = t_{90}$  for Run I (middle). We also show snapshots for the low- $\Sigma$  Run II (top) and the high- $\Sigma$  Run III (bottom) at  $t = 1.57 t_{\text{ff}}$  for their respective freefall times, when the stellar mass is at 90% and 87%, respectively. We show both projections along the  $z$ -axis onto the  $x$ - $y$  plane (left), as well as Hammer projections of the column density in rays starting 1.2 pc away from the stellar center of mass and continuing until the sphere intersects the outer edge of the box (right). The inner radius is chosen to omit a region of  $3^3$  voxels around the center of mass, while the outer radius is chosen such that all rays have the same radial extent, although some do not reach the edge of the simulation volume. The color scales show the surface density in units of  $M_\odot \text{pc}^{-2}$  (top) and the star particles as spheres, with the color scale (middle) showing the stellar mass in units of  $M_\odot$ .

filamentary that there is little difference between observing the cloud from outside and looking outward from its center.

Even as the effects of radiation feedback become more pronounced, the observed and circumcluster distributions remain similar, and both are close to lognormal. Figure 7 plots best-fit lognormal parameters for  $P_M$  as a function of time for both the observed and circumcluster PDFs for the fiducial model. From the lognormal fit to each PDF, we obtain a mean  $\mu_M = \langle \ln \Sigma \rangle_M$  and standard deviation  $\sigma_{\ln \Sigma} = \langle (\ln \Sigma - \mu_M)^2 \rangle_M^{1/2}$ . We define the

“cloud” surface density via  $\langle \Sigma \rangle_{\text{cloud}} = \exp(\mu_M - (1/2)\sigma_{\ln \Sigma}^2)$ , since this relation holds from the normalization of a lognormal. The mean cloud surface density steadily decreases with time (Figure 7(a)), while the best-fit variance remains approximately constant throughout star formation (Figure 7(b)).

To obtain the “cloud” mass  $M_{\text{cloud}}$ , excising low-density ambient and outflow mass, we integrate the best-fit lognormal, shown as a function of time in Figure 7(d). The best-fit lognormal distribution to  $P_M$  also gives us a way to estimate the

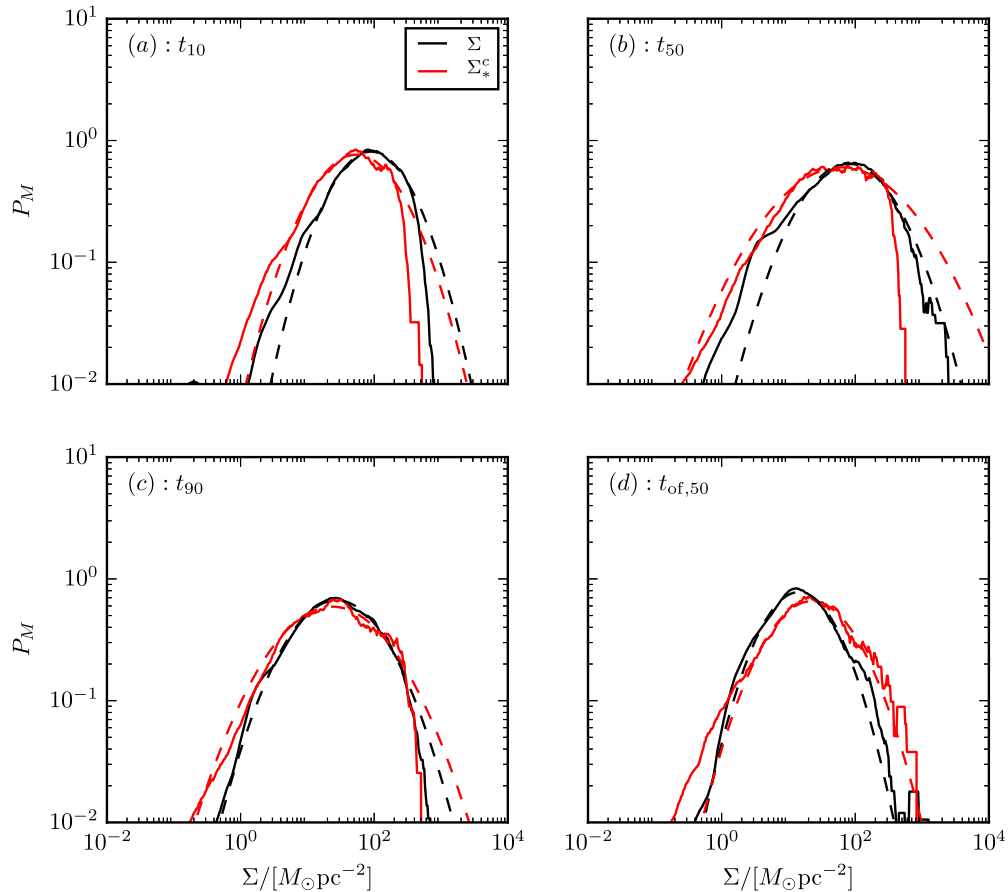


**Figure 6.** Surface density PDFs (by mass fraction) in the fiducial model at (a)  $t = 0.56t_{\text{ff}} = t_{10}$ , (b)  $t = 1.06t_{\text{ff}} = t_{50}$ , (c)  $t = 1.57t_{\text{ff}} = t_{90}$ , and (d)  $t = 2.17t_{\text{ff}} = t_{\text{of},50}$ . We show results for the observed surface density (black), and the circumcluster distribution beyond of the mean of the stellar distribution (red). In each case, we show both the simulated surface density distributions (solid lines) and the best-fit lognormal curves (dashed lines). In fitting lognormals, the 15% at low  $\Sigma$  is omitted since this is approximately the fraction that is unbound by the initial turbulence and so is already outflowing from the cloud. The 10% at high  $\Sigma$  is also omitted, since the distribution is poorly sampled there. For reference, with the opacity we adopt, the surface density is related to optical depth by  $\tau = 0.21\Sigma/(M_{\odot} \text{pc}^{-2})$ . With  $\tau = 1$  at  $\Sigma = 4.76 M_{\odot} \text{pc}^{-2}$ , well below the peaks in the mass PDFs, most of the mass is in structures that are quite optically thick to either external or internal FUV.

cloud’s effective volume and size. If we assume that the cloud is roughly spherical, then we can define an effective cloud radius  $r_{\text{eff}} = xr_0$  such that

$$\langle \Sigma \rangle_{\text{cloud}} \equiv \frac{M_{\text{cloud}}}{\pi r_0^2 x^2}. \quad (8)$$

Figure 7(c) shows the mean cloud expansion factor  $x$  over time, based on this definition and the lognormal fit, which gives a rough estimate of the effective cloud radius.

The character of the best-fit lognormal parameters appears to hold true across the full range of simulations. Table 2 shows  $\sigma_{\ln\Sigma}$  and  $x$  for the circumcluster surface density distribution at  $t_{10}$ ,  $t_{50}$ , and  $t_{90}$ . Almost regardless of surface density,  $\sigma_{\ln\Sigma} \sim 1.4\text{--}1.6$  and  $x \sim 1.2\text{--}1.6$ . Furthermore, the shape of  $P_M(\Sigma)$  does not change much in time, with  $\sigma_{\ln\Sigma}$  varying by only around 10%–20% from the beginning to the end of star formation.

We note that the mean values for  $\sigma_{\ln\Sigma}$  in the present simulations are high compared to some estimates of observed molecular clouds. For example, Schneider et al. (2015) measure the column density distributions for four GMCs in the Milky Way (correcting for line of sight contamination), and find  $\sigma_{\ln\Sigma}$  in the range 0.32–0.52, a factor  $\sim 4$  smaller than in our models. However, other current observational work suggests that variances may be nearly as large as those found in our

simulations, with Lim et al. (2016) finding  $\sigma_{\ln\Sigma} \sim 1.2\text{--}1.4$  in the IRDC G028.37+00.07, and emphasizing that results are sensitive to the detailed treatment of foreground and background corrections. Magnetization tends to limit compression by both turbulence and gravity, and preliminary results from magnetohydrodynamical (MHD) simulations we have conducted suggest that variances are somewhat lower than in the present (hydrodynamic-only) simulations. In addition, the mean temperature in molecular gas may in fact be closer to 20 K than the conventional value of 10 K that we have adopted (Heyer & Dame 2015); this would reduce  $\sigma_{\ln\Sigma}$  by a few tenths.

With lower  $\sigma_{\ln\Sigma}$ , based on the theory presented in Paper I, the expectation is that SFEs would be reduced, but qualitatively, the interaction between radiation and gas would be similar to the results we have found. Lower  $\sigma_{\ln\Sigma}$  would also imply that radiation could not escape from the cloud as easily. If the escape fraction of radiation were lower, this would increase the momentum transferred to the gas. With the cumulative absorption fraction  $\sim 50\%$  for the present models (see Section 5.3), this would be only a factor  $\sim 2$  difference. A reduced  $\sigma_{\ln\Sigma}$  would also reduce the variance in the velocity distribution of gas outflowing from the system because, as we show in Section 6, these quantities are directly related.

For an externally observed cloud, the mass distribution  $P_M(\Sigma)$  is complemented by the area distribution  $P_A(\Sigma)$ .

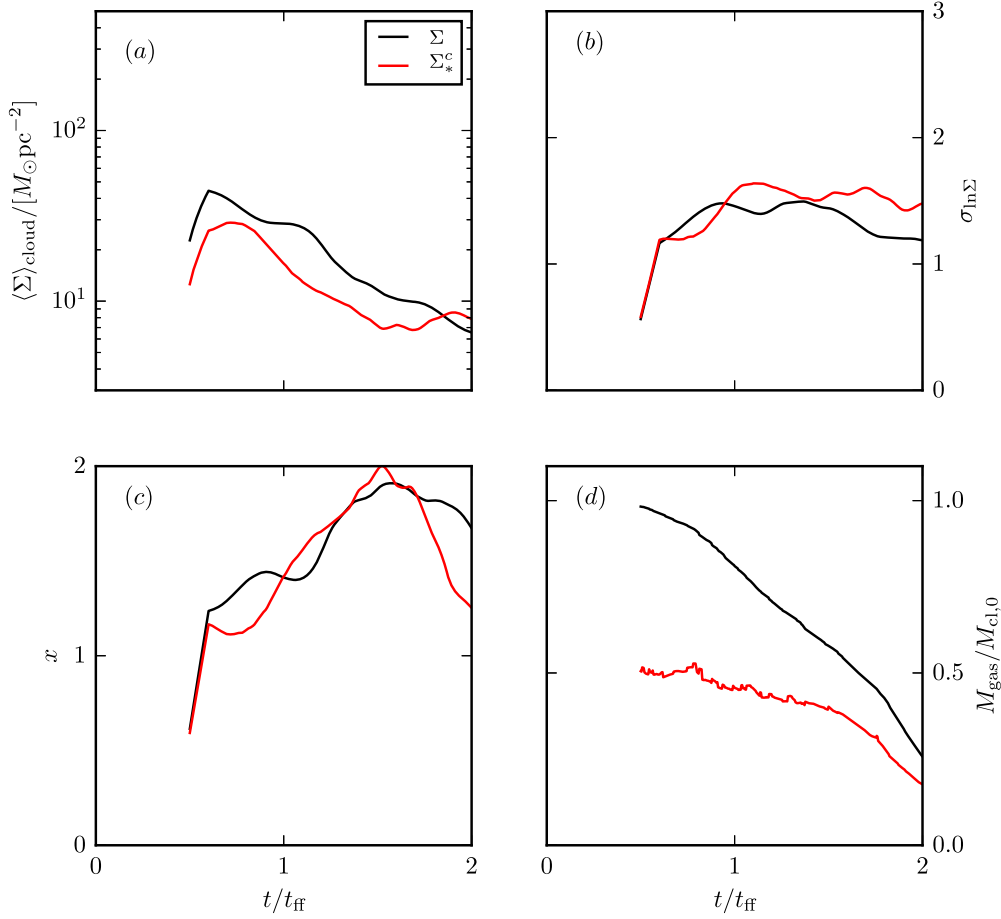


**Figure 7.** Best-fit lognormal parameters of surface density distributions in the fiducial model as a function of time. We show parameters for the fits for both observed surface density ( $\Sigma$ ) and circumcluster surface density ( $\Sigma_{*}^c$ ). In both cases, we show the best-fit mean cloud surface density  $\langle \Sigma \rangle_{\text{cloud}}$  (top left), lognormal standard deviation  $\sigma_{\ln \Sigma}$  (top right), the mean cloud expansion factor  $x$  (bottom left), and the total gas mass included in the fit (bottom right).

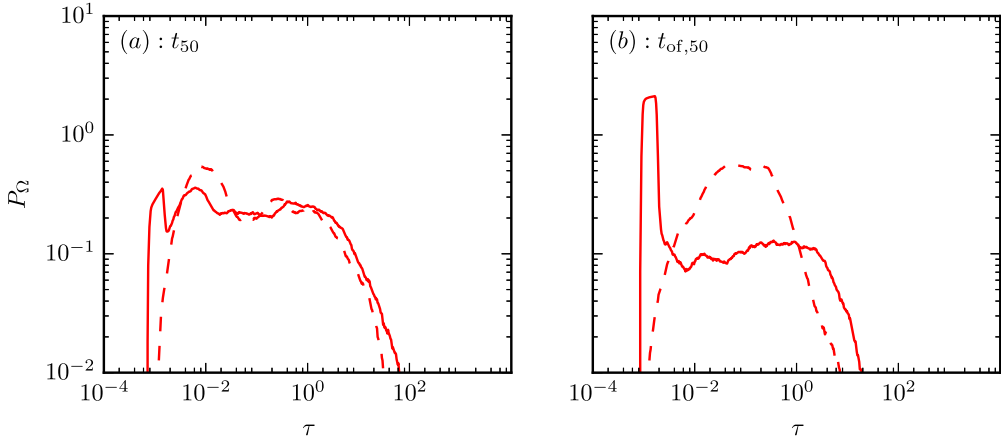


**Figure 8.** Optical-depth PDFs (by solid-angle fraction) at  $t_{50}$  and  $t_{\text{of},50}$ , for the fiducial model (solid curves) and a no-feedback model at the same times (dashed). We show results for the circumcluster distribution outside the mean radius of the stellar distribution. While most of the solid angle looking outward from the center of the stellar distribution is at  $\tau < 1$ , Figure 6 shows that in contrast, most of the mass is in optically thick structures.

However, in considering circumcluster distributions, there is no single area that characterizes any given ray because gas is at a range of distances. Instead, we can consider the distribution in solid angle  $\Omega$  with respect to the stellar center of mass. In addition, since this distribution is useful in characterizing how radiation is absorbed, we consider  $P_{\Omega}(\tau)$ , where the optical depth  $\tau$  is  $\kappa \Sigma_{*}^c$ . Since we adopt a constant  $\kappa = 1000 \text{ cm}^2 \text{ g}^{-1}$ ,

the PDFs in  $\tau$  are linearly related to PDFs in  $\Sigma_{*}^c$  using  $\Sigma_{*}^c / (M_{\odot} \text{pc}^{-2}) = 4.76\tau$ .

In Figure 8 we show the optical depth distributions at  $t_{50}$  and  $t_{\text{of},50}$ , for the fiducial model. Unlike the distributions in mass, these distributions in solid angle do not appear lognormal; instead, both during and toward the end of star formation, the PDFs are broad and double-peaked, with the peaks separated

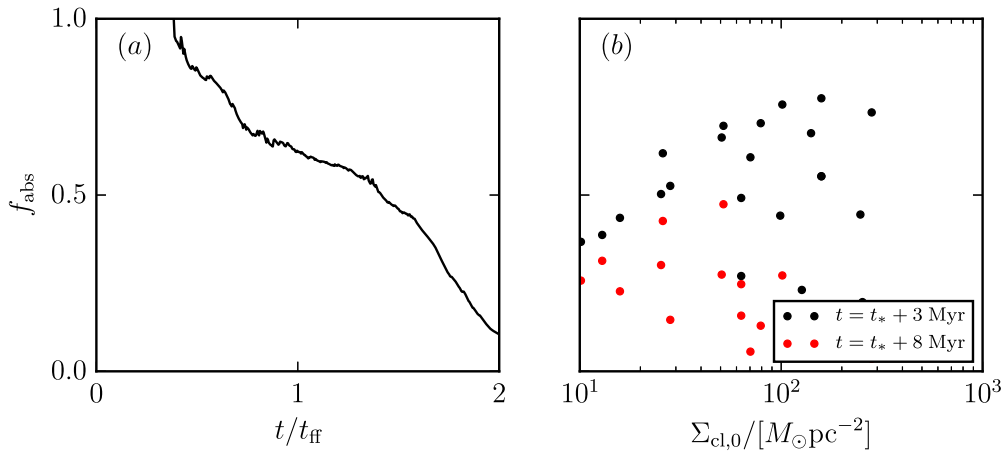


**Figure 9.** Absorption fraction, as defined in Equation (9), measured at the box radius as a function of time for the fiducial model (left). We also show  $f_{\text{abs}}$  as a function of model surface density for all models (right). Here,  $f_{\text{abs}}$  is measured 3 Myr (black) and 8 Myr (red) after star formation has begun in each model.

by more than two decades in  $\tau$ . This would be unsurprising for distributions of area as a function of optical depth (or of  $\Sigma$ ) for the externally observed case, because sightlines through the simulation domain sample both the cloud and the low-density ambient medium, creating a bimodal distribution. One might expect the “ambient-only” sightlines to disappear when looking outward from the center of the cloud; instead, the solid-angle distributions of  $\Sigma_{*}^c$  are even broader and flatter than the area distributions of “observed”  $\Sigma$ .

Comparison with  $\Omega$  distributions for the no-feedback case, also included in Figure 8, show that the bimodal PDF shape is not primarily a consequence of feedback. Instead, it reflects the fact that there are essentially two optical depth distributions: one for sightlines that pass through filaments, and one for sightlines that do not. Even without radiation forces clearing a path, there are natural channels in a turbulent cloud through which radiation may escape. We note that Dale et al. (2012, 2013) find a similar result, namely that large holes in their clouds were present even when ionizing feedback was turned off in their simulations.

Finally, we note that the effect of the large holes on  $P_M$  is minimal because they contain very little gas by mass. This also implies that they will have little effect on the momentum of gas outflows, since the same distribution is being accelerated outward. However, the holes have a large effect on the fraction of radiation escaping the cloud, as we discuss next.

### 5.3. Escape of Radiation

The gas surrounding the central cluster is highly filamentary, with large holes that allow radiation to escape. On the cloud or cluster scale, the amount of radiation absorbed helps to regulate star formation. For the present models, in which radiation is the only regulation mechanism, a higher escape fraction implies a lower Eddington ratio (since the total radiation force is  $\sim(1 - f_{\text{esc}})L/c$ ), which then requires a higher SFE and luminosity to disrupt the cloud. In Paper I, we found SFEs a factor of 10–20 higher than would naively be expected by simple considerations of the radiative force acting on a uniform shell. High escape fractions may partly explain this discrepancy.

Obtaining realistic estimates of radiation escape fractions from turbulent star-forming clouds is also important for understanding the ionization of the diffuse ionized gas in the Milky Way (e.g., Hoopes & Walterbos 2000; Voges &

Walterbos 2006), as well as cosmic reionization from UV escaping dwarfs galaxies at high redshift (e.g., Madau et al. 1999; Faucher-Giguère et al. 2008; Bunker et al. 2010; Kuhlen & Faucher-Giguère 2012). Although the present models do not directly address radiative transfer of ionizing radiation, the escape of non-ionizing UV is affected by similar factors.

We may characterize how porous our clouds are to UV radiation by measuring the outward radiative flux  $\langle F_r \rangle_{\Omega}$  in spherical shells around the center of mass. With  $L_{*}$  the total stellar luminosity, the absorption fraction at radius  $r$  is defined as

$$f_{\text{abs}}(r) \equiv 1 - 4\pi r^2 \langle F_r \rangle_{\Omega} / L_{*}, \quad (9)$$

where  $r$  is the radius of the sphere through which flux is computed. We note that another measure of the absorption fraction is  $f_{\text{abs}, \tau} \equiv \langle 1 - e^{-\tau} \rangle_{\Omega}$ ; for our models, this produces results that agree with  $f_{\text{abs}}$  within 10 or 15%.

Until  $\sim 1.5 t_{\text{ff}}$ , by which time the majority of star formation is complete, we find there is little difference between  $f_{\text{abs}}$  for models with and without feedback. This confirms the results of Section 5.2, i.e., that direct radiation pressure has little effect on internal cloud structure at early times, and is not effective at, for instance, driving the gas into thinner shells or filaments. Therefore, as with ionized gas pressure (Dale et al. 2012, 2013), radiation pressure only modifies the radiation escape fraction by  $\sim 5\%$ .

Figure 9(a) shows the evolution of  $f_{\text{abs}}$  measured at the box radius for the fiducial model, demonstrating that during the time when most of the stellar growth occurs,  $t/t_{\text{ff}} \sim 0.7$ – $1.6$ , the absorption fraction is relatively constant with roughly half of the radiation escaping the cloud. Considering now the full set of models, Figure 9(b) shows the absorption fraction as a function of initial cloud surface density at two set times after the onset of star formation: 3 Myr, when the first SNe could begin to explode, and 8 Myr, when the UV cluster luminosity is expected to drop to half its original value owing to the loss of O stars (Murray et al. 2005).<sup>2</sup> The values of  $f_{\text{abs}}$  at 3 Myr are also listed in Table 2.

A useful quantity is the cumulative absorption fraction up to a given time  $t$ , defined as the ratio of the total integrated flux

<sup>2</sup> Note, however, that the present simulations do not include SNe, nor do we allow the ratio of luminosity to mass to vary as a cluster ages.

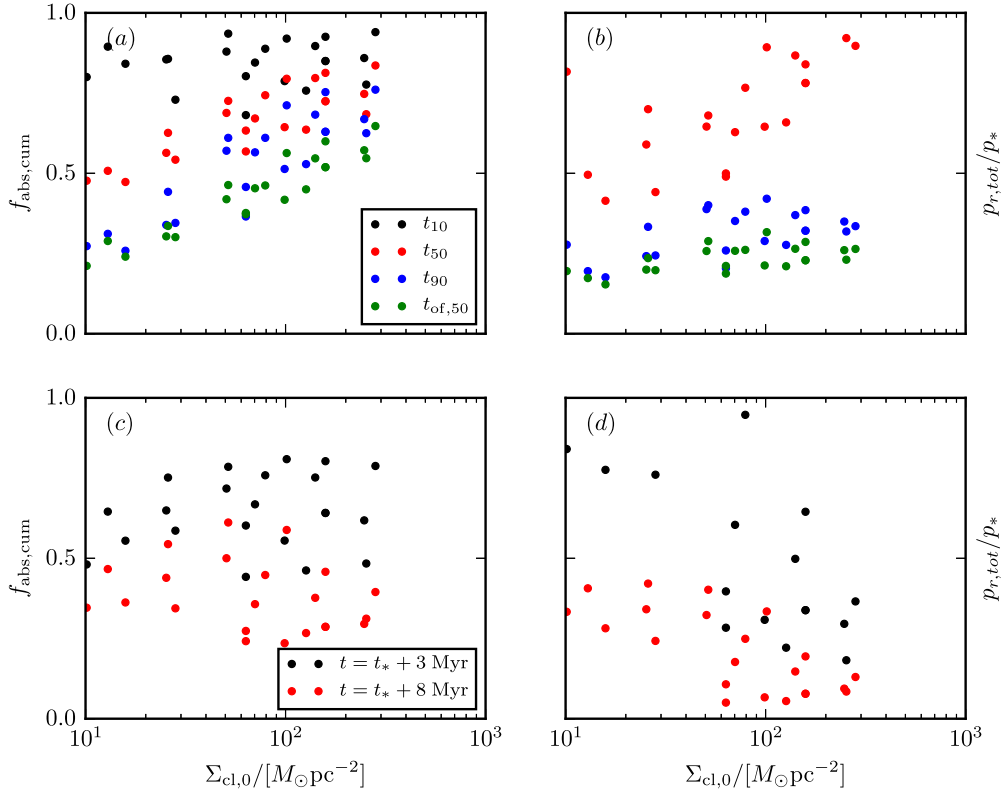


**Figure 10.** Cumulative absorption fraction (left) and ratio of the total radial gas momentum  $p_{r,\text{tot}}$  to total input stellar momentum  $p_*$  (right), each as a function of initial cloud surface density. In panels (a) and (b) we show values at four times: when the SFE is at 10% (black), 50% (red), and 90% (blue) of its final value, and when half of the final mass has escaped the box (green). In panels (c) and (d), we show values for 3 Myr (black) and 8 Myr (red) after star formation has begun in each model.

absorbed to the total input stellar luminosity, and computed via

$$f_{\text{abs,cum}}(t) = 1 - \frac{\int_0^t 4\pi r^2 \langle F_r \rangle_{\Omega} dt}{\int_0^t L_* dt}. \quad (10)$$

This quantity is plotted for several evolutionary stages and at two specific times in Figure 10. We also show for comparison the ratio of the total radial momentum of gas,  $p_{r,\text{tot}}$ , to the total input momentum in stellar radiation,  $p_* = \int dt L_*/c$ . Here the total radial momentum of the gas is defined as  $p_{r,\text{tot}} = p_{r,\text{box}} + p_r$ , which consists of the component contained within the simulation volume,  $p_{r,\text{box}} = \int \rho \mathbf{v} \cdot \hat{\mathbf{r}} d^3x$ , added to the time-integrated outflowing gas momentum  $p_r = \int dt \int \rho (\mathbf{v} \cdot \hat{\mathbf{r}})^2 r^2 d\Omega$ , both defined with reference to the stellar center of mass. Both the cumulative absorption fraction and the momentum ratio represent the efficiency of converting radiation momentum to gas momentum.

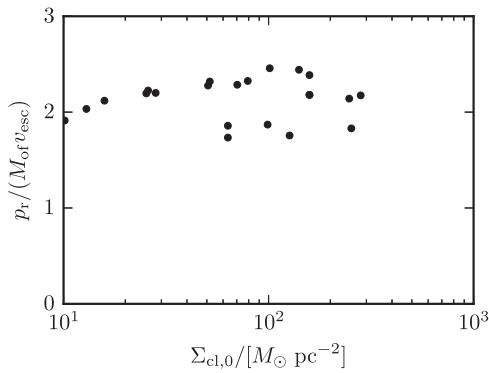
By definition,  $f_{\text{abs,cum}} < 1$ , and from conservation of momentum in an idealized spherical system (with zero initial velocities), the value of  $f_{\text{abs,cum}}$  at late times should approach  $p_{r,\text{tot}}/p_*$ . Of course, our model clouds are not ideal in that some flux is cancelled in the decentralized stellar distribution and since a small amount of momentum is also carried outward by the  $\sim 12\%$  of gas mass that is unbound by the initial turbulence. More importantly, at earlier times, the initial turbulence in the box can contribute non-negligibly to the measured  $p_{r,\text{tot}}/p_*$ ; this explains why some values of  $p_{r,\text{tot}}/p_*$  at 3 Myr (as listed in

Table 2) can exceed unity, especially in low-density clouds with correspondingly long freefall times.

The values of the cumulative absorption fraction are on average higher than their instantaneous counterpart, but the difference is only  $\sim 50\%$ . Thus, although most of the radiation is absorbed at the earliest times, this stage is brief, and the luminosity is lowest then. We also note that the trends with surface density remain the same. In particular, regardless of the initial cloud surface density, the cumulative absorption fraction is  $\sim 60\%$  by 3 Myr and  $\sim 30\%$  by 8 Myr. At late times, the radial momentum of the gas is  $\sim 25\%$  of the level it would reach had the radiation field been spherically symmetric and perfectly absorbed (see Figure 10(b)).

Our results on absorption fraction differ from those of Dale et al. (2012, 2013), who find that for molecular clouds dominated by ionized gas pressure, the absorption fraction generally increases with surface density (offsetting higher SFE), and most cases therefore contribute roughly the same ionizing luminosity to the ISM. The difference is probably not due to differences in feedback, since neither our study nor theirs find much change in internal cloud structure as a result of early feedback. Instead, it may arise from the fact that they generally consider clouds with a lower surface density with freefall times much longer than 3 Myr, hence they may not have yet been dispersed by that time. The one cloud with a higher surface density they model has an absorption fraction of only  $\sim 10\%$  by 3 Myr.

Finally, we note that the discrepancy between the absorbed and input radiation is not enough to account for the high SFE of our simulated clouds. Simple models of cloud destruction, which posit that star formation stops when the mean cloud



**Figure 11.** Mass-weighted mean velocity of outflowing gas as a function of initial cloud surface density. For comparison, we normalize to the initial escape speed of each model cloud.

surface density reaches the Eddington surface density, would estimate for our fiducial model an efficiency of  $\varepsilon \sim 0.03$ , a factor of  $\sim 10$  smaller than the SFE obtained in our simulation. An extra factor of 2 due to escaping radiation is therefore not sufficient to explain why gas remains bound and continues to form stars. Instead, the reason for the high SFE is that radiation momentum is not equally distributed to all of the mass in the cloud. Low- $\Sigma$  structures with large solid angles (per unit mass) intercept much more radiation than required to reach escape speed from the cloud, whereas high- $\Sigma$  structures continue contributing to star formation until the luminosity and corresponding radiation flux are finally sufficient to expel and unbind them.

## 6. Gas Outflows

We have established that the net radial momentum of the gas at late times is significantly lower than the total radiation momentum input from stars, owing to the relatively high radiation escape fraction (Figure 10(b)). Figure 11 directly shows the ratio of outflowing gas momentum to outflowing gas mass, in units of the escape speed at the cloud’s initial radius (both momentum and mass outflows are integrated over the duration of the simulation). Evidently, the outflowing gas is unbound, and in fact, the (scaled) mean velocity of the outflowing gas is relatively constant across our full range of simulations, in the range  $p_r / (M_{\text{of}} v_{\text{esc}}) \sim 1.5\text{--}2.5$  for all models. However, of equal interest is the distribution of momenta and velocities for the escaping gas; i.e., to what extent does radiation pressure drive fast low-density outflows versus slow high-density outflows in a given system?

Characterizing the properties of outflows driven by radiation pressure is particularly interesting in connection to the origin of “cool” fast winds from starburst galaxies (note that unlike in the ISM, in this context “cool” means  $T < 10^6$  K). These winds emerge at velocities of up to  $\sim 1000$  km  $s^{-1}$ , and are seen in gas that is cool enough to show absorption in NaD or Mg II. The origin of this high-velocity cool material is not understood (Veilleux et al. 2005). Possibilities include entrainment of dense clouds (e.g., Scannapieco & Brügger 2015) by the outflowing hot gas created by supernova explosions (e.g., Chevalier & Clegg 1985), or radiative cooling of hot outflows that are themselves sufficiently dense (e.g., Wang 1995; Thompson et al. 2016), or acceleration by radiation pressure forces acting on cloudlets exposed to the combined radiation field of thousands of luminous stars created in a starburst

(e.g., Murray et al. 2005; Thompson et al. 2015). Although the present simulations do not study clusters as massive as those powering starbursts, they do provide valuable insight into the driving of winds by radiation pressure, as the interaction of radiation and gas is implemented here via fully self-consistent RHD.

Thompson & Krumholz (2016) have pointed out that when considering wind driving by radiation pressure, the lognormal distribution of density is important because structures of low surface density may be super-Eddington even when the circumcluster gas distribution as a whole is not. In our simulations, as the luminosity increases over time, an increasing fraction of the gas becomes super-Eddington and is driven out of the cloud, until the last remnants are swept clean. Thompson et al. (2015) argue that the asymptotic velocities of structures accelerated by a luminous source will depend on both the source luminosity and the distance at which they become optically thin, and that for certain parameter regimes, velocities can be much greater than the escape speed of the system. We can use our RHD simulations to test these and other ideas related to the properties and statistics of radiation-driven winds from turbulent, cold, star-forming gaseous systems.

We consider first the velocity distribution of gas both in the cloud and escaping it. In Figure 12 we show the PDF of mass as a function of velocity, both absolute and radial, for gas in the fiducial model at various stages of evolution. At early times, the radial velocity distribution is very close to the Gaussian distribution of our initial turbulent field, with slight excesses at negative velocities corresponding to gas accreting onto the central star and at positive velocities corresponding to gas being driven from the cloud. However, once star formation feedback becomes significant, the distribution of velocities above the escape velocity of the cloud,  $v_{\text{esc}} \sim 5.4$  km  $s^{-1}$ , departs dramatically from this Gaussian shape.

To understand the distribution of high-velocity gas, we first consider the relationship between velocity and surface density on individual rays emerging from the stellar center of mass. In Figure 13(a) we show the mean mass-weighted velocity along sightlines as a function of their surface density. The radial velocity for a given surface density bin is calculated by computing the net radial momentum of gas along all rays within that bin, then dividing by the total mass along those rays.

The relationship between surface density and velocity can be understood by considering individual structures interacting with a central source of radiation and gravity, becoming unbound when their Eddington factors exceed unity. We follow the motion of a structure initialized (from rest) at radius  $r_0$  with surface density  $\Sigma_0$ . We assume the structure remains within a fixed solid angle with respect to the source, so that as it moves outward, its surface density decreases with distance  $r$  as  $\Sigma = \Sigma_0 (r_0/r)^2$  (note that we simply use  $\Sigma$  for this idealized ballistic calculation, reserving  $\Sigma^c$  for circumcluster surface densities measured in our simulations). The inward gravitational acceleration from the star cluster is  $GM_*/r^2$ , while the outward radiation force per unit mass is  $\Psi M_*(1 - \exp(-\tau)) / (4\pi c \Sigma_0 r_0^2)$ . Here, we have used  $L_* = \Psi M_*$  for the cluster luminosity, and the optical depth of the structure is  $\tau = \kappa \Sigma = \tau_0 (r_0/r)^2$  for  $\tau_0 = \kappa \Sigma_0$ .

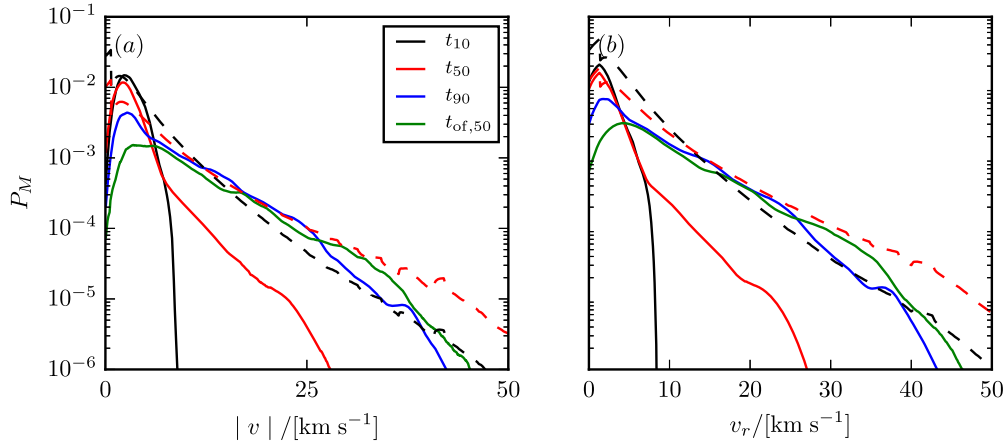


**Figure 12.** Probability density functions of the velocity in our fiducial simulation for both the absolute velocity (left) and the radial velocity away from the center of mass (right). We show results at  $t/t_{\text{ff}} = 0.56, 1.06, 1.57,$  and  $2.17$ , corresponding to  $t_{10}, t_{50}, t_{90},$  and  $t_{\text{of},50}$ . We also show theoretical velocity distributions obtained by applying Equation (17) with a best-fit lognormal distribution over surface density to two assumed density profiles: uniform (black dashed), and  $r^{-1}$  (red dashed), respectively.

The equation of motion then becomes

$$\begin{aligned} \frac{dv}{dt} &= \frac{\Psi M_*}{4\pi c \Sigma_0 r_0^2} (1 - e^{-\tau}) - \frac{GM_*}{r^2} \\ &= \frac{GM_*}{r_0^2} \left[ \frac{\Sigma_{\text{E,max}}}{\Sigma_0} (1 - e^{-\tau_0(r_0/r)^2}) - \left(\frac{r_0}{r}\right)^2 \right], \end{aligned} \quad (11)$$

where we have introduced a maximum Eddington surface density

$$\Sigma_{\text{E,max}} \equiv \frac{\Psi}{4\pi c G} = 380 M_\odot \text{ pc}^{-2} \left( \frac{\Psi}{2000 \text{ erg s}^{-1} \text{ g}^{-1}} \right). \quad (12)$$

The quantity  $\Sigma_{\text{E,max}}$  represents the highest surface density for which the stellar Eddington ratio

$$\begin{aligned} f_{\text{Edd},*} &\equiv \frac{F_{\text{rad}}}{F_{\text{grav},*}} = \frac{\frac{\Psi M_*}{4\pi c r^2} (1 - e^{-\tau})}{\frac{GM_* \Sigma}{r^2}} \\ &= \frac{\Sigma_{\text{E,max}}}{\Sigma} (1 - e^{-\tau}) \end{aligned} \quad (13)$$

can be higher than unity, so that the radiation force overcomes gravity. Thus, only structures with  $\Sigma < \Sigma_{\text{E,max}}$  can be accelerated outward. We note that in reality, an accelerating fluid element will feel the gravity of the full remaining cloud mass, not just the central star cluster. However, once most of the cloud mass has been expelled, this is a small correction. In fact, at the point the fluid element becomes unbound and its radius begins to increase, even the stellar gravity term becomes negligible compared to the radiation term. To see this, note that while the structure remains optically thick, the radiation force in Equation (11) is constant, while gravity  $\propto r^{-2}$ . If the structure becomes optically thin, taking  $\tau \ll 1$  in Equation (13) shows that the Eddington ratio approaches a maximum value given by

$$\begin{aligned} f_{\text{Edd},*,\text{max}} &= \kappa \Sigma_{\text{E,max}} \equiv \tau_{\text{E,max}} \\ &= 80 \left( \frac{\Psi}{2000 \text{ erg s}^{-1} \text{ g}^{-1}} \right) \left( \frac{\kappa}{1000 \text{ cm}^2 \text{ g}^{-1}} \right), \end{aligned} \quad (14)$$

which is large for our fiducial parameters. Provided that star formation is slow compared to the time to accelerate gas out of the cloud (i.e., provided the acceleration timescale is short compared to the freefall time), we can also treat  $M_*$  as a constant in Equation (11).

Multiplying Equation (11) by  $v = dr/dt$ , we integrate over  $t$  to obtain the velocity as a function of distance  $r$ , given by

$$\begin{aligned} \frac{v^2(\Sigma_0, r)}{v_{\text{esc}}^2(r_0)} &= \frac{\tau_{\text{E,max}}}{\tau_0} \left\{ \sqrt{\tau_0} \pi \left[ \text{erf}(\sqrt{\tau_0}) - \text{erf}\left(\frac{\sqrt{\tau_0}}{r/r_0}\right) \right] \right. \\ &\quad \left. + \frac{r}{r_0} [1 - e^{-\tau_0(r_0/r)^2}] + e^{-\tau_0} - 1 \right\} + \frac{r_0}{r} - 1. \end{aligned} \quad (15)$$

Here, we include only the star cluster mass in  $v_{\text{esc}}(r_0) \equiv (2GM_*/r_0)^{1/2}$ . Note that Equation (15) may also be used to write the velocity in terms of the surface density  $\Sigma$  at a distance  $r$  by substituting  $\tau_0 = \kappa \Sigma r^2 / r_0^2$ .

At large distances from the source  $r/r_0 \gg 1$ ,

$$\begin{aligned} v^2(\Sigma_0) &\rightarrow v_{\text{esc}}^2(r_0) \left\{ \frac{\tau_{\text{E,max}}}{\tau_0} [\sqrt{\tau_0} \pi \text{erf}(\sqrt{\tau_0}) \right. \\ &\quad \left. + e^{-\tau_0} - 1] - 1 \right\}. \end{aligned} \quad (16)$$

Therefore, structures that start as optically thin ( $\tau_0 \ll 1$ ) have  $v/v_{\text{esc}} \rightarrow (\tau_{\text{E,max}} - 1)^{1/2} \approx 9$ , while structures that start as optically thick ( $\tau_0 \gg 1$ ) eventually become optically thin at  $r/r_0 = \tau_0^{1/2}$  and reach a final speed  $v/v_{\text{esc}} \rightarrow [\tau_{\text{E,max}}(\pi/\tau_0)^{1/2} - 1]^{1/2}$ . That is, structures that are initially optically thin accelerate to a velocity nearly 10 times the escape speed at their launch point, while this is reduced by a factor  $\sim (\pi/\tau_0)^{1/4}$  for structures that are initially optically thick. For our parameter choice  $\kappa = 1000 \text{ g cm}^{-2}$ , the  $\tau = 1$  transition between optically thick and thin occurs at a surface density of  $\Sigma_{\text{th}} = \kappa^{-1} = 4.8 M_\odot \text{ pc}^{-2}$  (or hydrogen column  $N_{\text{th}} = 4.3 \times 10^{20} \text{ cm}^{-2}$ ). Because optical depth decreases  $\propto r^{-2}$ , the asymptotic velocity in the optically thick limit is essentially the same as obtained by taking the optically thin limit for a launch radius where the optical depth is equal to  $\pi$ . We note

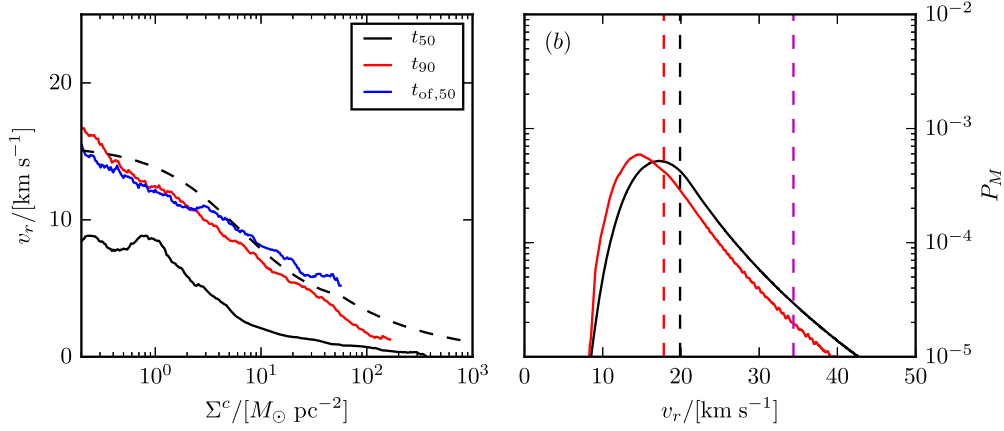


**Figure 13.** Left: mean radial outflow velocity as a function of circumcluster surface density at different stages in the evolution of the fiducial model, calculated as the total momentum along a radial sightline divided by the total gas mass. We overplot the expected velocity (black dashed line) calculated using Equation (15) with  $M_* = \varepsilon_{\text{final}} M_{\text{cl},0} = 0.42 M_{\text{cl},0}$ ;  $r_0 = r_{\text{cl},0}$ ; and  $r = 2r_{\text{cl},0}$ . We omit  $\Sigma^c < 0.1$  since these surface densities consist of primarily the lowest density gas that has generally dropped below the computational density floor and was reset to a minimum density and zero velocity. Right: mass distribution as a function of asymptotic outflow velocity, using Equation (17) with both a best-fit lognormal surface density distribution (black) and the full simulated surface density distribution when  $t = 0.57 t_{\text{ff}}$  (red), with  $\rho(r) \propto r^{-1}$  and only considering surface densities such that  $\Sigma^c < \Sigma_{\text{E,max}}$ . Dashed vertical lines show the mean velocity in each case, as well as the velocity expected for expansion of a uniform shell (magenta).

that Equation (12) imposes a limit  $\tau_0 < \tau_{\text{E,max}}$  on the optical depth of structures that can be accelerated at all, implying a lower limit on the velocity of escaping structures at large distance:  $v/v_{\text{esc}}(r_0) > [(\pi\tau_{\text{E,max}})^{1/2} - 2]^{1/2} \sim 3.7$ . Thus, there is a range of only about a factor of two between the minimum and maximum asymptotic velocities for structures originating at a given radius  $r_0$ . However, structures that begin with optical depth near  $\tau_{\text{E,max}}$  would require an order of magnitude increase in radius to reach their asymptotic velocity. In practice, this asymptotic velocity may not be reached unless the cluster and cloud are relatively isolated within their environment.

For our simulations, acceleration starts at  $r_0 \lesssim r_{\text{cl},0}$  and continues until the gas leaves the box at  $r \sim 2r_{\text{cl},0}$ . We may therefore compare expectations of radiative acceleration to our simulation results by plotting Equation (15) for  $r = 2r_{\text{cl},0}$ ,  $r_0 = r_{\text{cl},0}$  and  $M_* = 0.42M_{\text{cl},0}$  (corresponding to the final stellar efficiency of the fiducial model). Here, we take care to adjust for the fact that by the time fluid elements reach the edge of the box, the circumcluster surface density  $\Sigma^c \sim \Sigma_0/4$  (we also omit the asterisk subscript in  $\Sigma_*^c$  since at late time the circumcluster material is well outside the star particle distribution). The resulting predicted relationship between  $v$  and  $\Sigma^c$  is shown in Figure 13, compared to the measured relationship between mean velocity and  $\Sigma^c = \int \rho dr$  obtained along lines of sight in the simulation at various stages. We see that Equation (15) captures the late-time relationship between velocity and surface density well. The match is poor at early times, but this is as expected since our plotted data use the final stellar mass and the gas has not yet had a chance to expand to the edge of the box. Notably, the simulation results are generally consistent with the predicted power-law relation between  $v$  and  $\Sigma^c$  at high surface density (corresponding to the  $v \propto (\Sigma^c)^{-1/4}$  behavior expected in the optically thick limit).

For comparison to the distribution of velocity with mass shown in Figure 12, we consider the full range of launch points  $r_0$  and the PDF of  $\Sigma^c$  by mass at each launch point. A structure of given  $\Sigma_0$  will accelerate to higher asymptotic velocity if it is launched from  $r_0$  nearer to the cluster center. Conversely, a fluid element starting with low  $\Sigma_0$  and large  $r_0$  may be able to reach the same asymptotic velocity as a fluid element starting from high  $\Sigma_0$  at

small  $r_0$ . In particular, starting from optically thick conditions (as is true for most of material in the cloud), Equation (16) shows that the asymptotic velocity scales as  $v \propto r_0^{-1/2} \Sigma_0^{-1/4} M_*^{1/2}$ , i.e., inversely with the fourth root of gas mass per unit solid angle (and directly with the square root of the cluster mass). Thus, to obtain  $P_M(v)$ , we must consider the fraction of mass at each radius in the cloud that is in structures of a given surface density, and integrate over the distribution of mass with radius.

For the distribution of mass with radius, we adopt the spherically symmetric power-law density profile in radius  $\rho(r) \propto r^{-\alpha}$  discussed in Section 4.1. The distribution of possible starting radii is then  $P_M(r_0)dr_0 = dM/M \propto r_0^{2-\alpha} dr_0$ , which leads to a mass-weighted mean value of inverse radius equal to  $r_{\text{cl}}^{-1}(3-\alpha)/(2\alpha)$ . Equation (15), which represents  $P_M(v|\Sigma_0, r_0)$ , may then be used to derive the theoretical distribution of outflow velocity by marginalizing over our initial lognormal distribution for  $\Sigma_0$  and the assumed distribution for  $P_M(r_0)$  to obtain

$$P_M(v)dv = \int dr_0 \int d\Sigma_0 P_M(v|\Sigma_0, r_0) P_M(r_0) P_M(\Sigma_0) dv, \quad (17)$$

where we have assumed the independence of  $\Sigma_0$  and  $r_0$ . The resulting outflow velocity distribution (taking  $r = 2r_{\text{cl},0}$ ), shown in Figure 12 for  $\alpha = 0$  (uniform-density distribution) and  $\alpha = 1.0$  (best-fit to our simulations), compares remarkably well to the final velocity distribution. Necessarily, we do not capture the distribution below  $v_{\text{esc}}$  since we are only considering outflows. Furthermore, we overestimate the mass in the high-velocity tail since the theoretical distribution, which uses the surface density distribution at the onset of star formation, does not account for mass leaving the simulation volume. This becomes quite pronounced by the time half the mass has left the box. However, at velocities below this tail (and above  $v_{\text{esc}}$ ), the theoretical prediction captures the shape of the distribution obtained in the simulation rather accurately.

Given how well the simple theoretical model matches the measured velocity distributions in the “near” region (i.e., within our computational domain), it is interesting to apply it to predict asymptotic velocities at large distance. Adopting a density profile  $\rho \propto r^{-1}$  within the cloud, Figure 13(b) shows what the

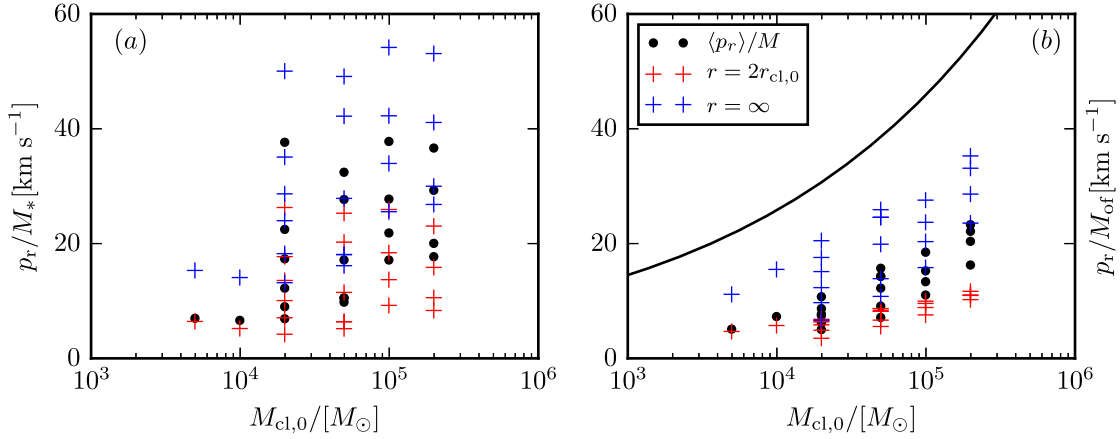


**Figure 14.** Outflowing gas momentum generated by direct radiation pressure per unit stellar mass formed (left) and per unit outflowing mass (right) as a function of initial cloud mass. Results from all models are shown (black dots). For comparison, we also show the theoretical mean velocities (crosses) based on Equations (15) and (17) at  $r = 2r_{\text{cl},0}$  (red) and for  $r \rightarrow \infty$  (blue), as well as the equivalent final velocity for a uniform shell from Equation (18), with  $\varepsilon = 0.5$  (black line).

distribution would become if all gas were accelerated until it becomes optically thin, using Equation (17) and the fiducial model’s surface density distribution  $P_M(\Sigma^c)$  at  $t_{10}$ . Around 99% of the mass in the fiducial model is below a velocity of  $\sim 40 \text{ km s}^{-1}$  or close to eight times the escape velocity from the original edge of the cloud. Although the PDFs of cloud material have a slight excess above a lognormal at low  $\Sigma$  (e.g., see Figure 6), this does not result in any significant difference in the outflow velocity distribution because it represents very little mass. The peak of the distribution in Figure 13(b) has a roughly lognormal shape because the relationship between asymptotic velocity and surface density is  $v \propto \Sigma_0^{-1/4}$  for optically thick structures (most of the material), and the underlying  $P_M(\Sigma_0)$  is lognormal.

In our simulations, most of the gas mass is in structures that are optically thick to UV, i.e., with  $\Sigma^c > \Sigma_{\text{th}} = \kappa^{-1} \sim 4.8 M_\odot \text{ pc}^{-2}$ . This is also true by definition in real molecular clouds, because at lower column, molecules would be dissociated by UV. Only the small amount of gas that begins in optically thin structures will reach velocities as high as  $\sim 9v_{\text{esc}}(r_0)$ . In contrast, most of the gas begins in optically thick structures, becoming optically thin only at distances where  $v_{\text{esc}}(r_0)$  has dropped below that of the original cloud (i.e., for  $r > r_{\text{cl},0}$ ), and would therefore have lower asymptotic “wind” velocity. Owing to the lognormal distribution, with most of the mass at surface densities well above the mean value for the cloud, these structures would accelerate more slowly and reach lower final speeds than would be true for a uniform-density cloud. For the fiducial model, accounting for the lognormal distribution, the predicted mean outflow velocity would be lower than  $20 \text{ km s}^{-1}$  (Figure 13b). By comparison, if an optically thick shell of mass  $(1 - \varepsilon)M_{\text{cl},0}$  uniformly distributed in solid angle were accelerated outward by radiation from a cluster of mass  $\varepsilon M_{\text{cl},0}$ , it would reach an asymptotic velocity (see Equation (16)) given by

$$v_{\text{unif}} \rightarrow \left(\frac{\Psi\varepsilon}{c}\right)^{1/2} \left(\frac{\kappa M_{\text{cl},0}}{1 - \varepsilon}\right)^{1/4}, \quad (18)$$

which would be  $\sim 35 \text{ km s}^{-1}$  for the fiducial model. While these overall scalings with cloud mass and SFE are still expected to apply,<sup>3</sup> the lognormal density distribution in the

cloud tends to reduce the mean value of the “wind” velocity, while broadening the overall distribution. Even though velocities are lower than the naive prediction, radiation is still capable of driving outflows at a mean final velocity of 3–4 times the initial escape velocity from the cloud’s surface. Note that this is roughly twice as high as the mean value  $p_r/(M_{\text{of}} v_{\text{esc}}) \sim 2$  shown in Figure 11 as measured from our simulations, because acceleration would continue outside of our simulation domain.

Our conclusion that non-uniform surface density systematically lowers the mean outflowing gas velocity holds true across the cloud mass and radius variations explored in our simulations. In Figure 14 we show the mean radially outflowing cloud momentum per unit outflow mass (i.e., the mean outflowing gas velocity) and per unit stellar mass, as functions of the initial cloud mass. In all cases, the theoretical outflow velocity predicted by Equation (15), when integrated over the best-fit lognormal surface density distribution and power-law density profile via Equation (17), captures the simulated momentum per unit outflow mass reasonably well. The estimate is slightly less accurate at higher cloud masses because of the effect of outflows caused by turbulence in the initial conditions (this causes more bias in high-mass clouds because the radiation-driven outflows are a smaller fraction of the total).

Finally, we note that based on the statistical properties of our simulations and the radiation acceleration model, the value of the outflow momentum in gas per stellar mass formed,  $p_r/M_*$ , is expected to be in the range 20–80  $\text{km s}^{-1}$  (the model includes acceleration beyond the simulation box, and therefore yields values higher than reported in Table 2). This is far below the simple estimates of the momentum injection by radiation forces often adopted in the literature, which use  $p_r/M_* \sim 180 \text{ km s}^{-1}$  based on the assumption that all the radiation over the lifetime of a cluster is absorbed. There are several factors that contribute to this reduction: (a) a large fraction of the radiation escapes owing to the highly inhomogeneous gas distribution created by turbulence, (b) the increase in mass-weighted mean surface density (again due to turbulence) reduces the acceleration of fluid elements, and (c) any individual gas structure becomes optically thin as it expands away from the cluster, thus limiting the total radiation it absorbs. The low values of  $p_r/M_*$  from this process compared to that for radiative supernova remnants

<sup>3</sup> From Equation (12),  $\Sigma^c < \Sigma_{\text{E,max}}$  is required for the ejection of any given structure, and if the final SFE is controlled by radiation, this implies a value for  $(1 - \varepsilon)M_{\text{cl},0}/r_0^2$  that depends in detail on the lognormal distribution (Paper I). In terms of overall scalings, this leads to  $M_{\text{cl},0}^{1/4}/(1 - \varepsilon)^{1/4} \propto v_{\text{esc}}(c/G\Psi)^{1/4}$ .

( $\sim 3000 \text{ km s}^{-1}$ ; e.g., Kim & Ostriker 2015) implies that momentum injection by UV radiation is not important to driving turbulence or otherwise providing dynamical support to the bulk of the ISM in galaxies. Nevertheless, UV radiation may still play an important role in accelerating a small fraction of the gas to high velocities ( $\gtrsim 100 \text{ km s}^{-1}$ ) in starbursts, as Equations (16) and (18) suggest for regions with a high mass ( $\sim 10^7\text{--}10^8 M_\odot$ ) in luminous stars and a high escape speed.

## 7. Summary and Discussion

In Paper I we presented the first results from a set of simulations that study gravitational collapse, star formation, and gas dispersal by UV radiation forces in turbulent GMCs. There, we characterized the distributions of the gas column density produced by turbulence as lognormal PDFs, analyzed the dependence of the SFR and final SFE on cloud properties, and related the final SFE in each cloud to the properties of the PDF via the condition that the outward radiation force must exceed the inward gravitational force for individual dense structures to be ejected. Here we further consider aspects of cloud structure produced by turbulence combined with self-gravity, and investigate the implications of this structure for the interaction with radiation from embedded star clusters. We use our simulations to quantify the escape of stellar UV radiation from filamentary clouds in which star clusters are born, to measure the total momentum transfer from radiation to gas, and to examine the detailed distribution of mass with velocity in the outflowing gas. Our main conclusions are as follows:

1. *Cloud evolution and star clusters.* The clouds in our simulations are highly inhomogeneous throughout their evolution, with most of the mass concentrated in dense filaments and star formation exclusively within these structures. Radiation emerging from embedded clusters removes the lower density gas from the cloud, creating large holes through which radiation can escape. At early times (until at least halfway through the star formation process), the overall density profile of gas in the cloud is fairly shallow, having  $\rho \propto r^{-\alpha}$  with  $\alpha \sim 0.8\text{--}1.3$  (see Figure 2). Since all models in this work are initialized with the same virial parameter ( $\alpha_{\text{vir}} = 2$ ), corresponding to a marginally gravitationally bound cloud, they show only a mild increase in cloud size until they are eventually dispersed by radiation pressure.
2. *Circumcluster surface density distribution.* Analytical models proposed recently by Thompson & Krumholz (2016) and in Paper I suggest that the SFE and properties of radiation-driven outflows from star-forming regions are strongly affected by turbulence, which establishes the distribution of gas densities. For clouds with centrally concentrated stars, the relevant distributions are the PDFs (by mass and by solid angle) as a function of circumcluster surface (or column) density. If most of the mass is in structures well above the mean surface density, a GMC can simultaneously drive low-density outflows while continuing to form stars well beyond the point at which a uniform cloud would nominally become super-Eddington.

We find that the circumcluster distribution by mass is quite similar to the observed column density distribution, as might be expected for a highly filamentary cloud, and it is reasonably well fit by a lognormal with  $\sigma_{\ln \Sigma} \sim 1.4$

across all clouds. Moreover, we find (similar to Dale et al. 2012, 2013 for the case of ionizing radiation) that the shape of the mass PDF is virtually unaffected by radiation feedback up to late times. As a result, much of the mass in the cloud is sub-Eddington even when the cloud has an average Eddington factor above unity. In fact, star formation in our models only halts when the mean value of  $f_{\text{Edd}} \sim 10$  is reached, i.e., radiation pressure becomes a factor of 10 stronger than gravity (see Figure 4). This is substantially different from the assumptions of most analytical models (e.g., Murray et al. 2005, 2010; Krumholz & Matzner 2009; Fall et al. 2010; Kim et al. 2016), which infer a much lower SFE by assuming that star formation halts once the mean Eddington factor of  $f_{\text{Edd}} = 1$  is attained.

As a caveat, we note that our values of  $\sigma_{\ln \Sigma}$  may be somewhat higher than is typical in real star-forming GMCs, although the observational situation remains controversial. Since the values of  $f_{\text{Edd}}$  and the SFE required to halt star formation increase with  $\sigma_{\ln \Sigma}$ , realistic values might be lower than we find here.

3. *Escaping radiation and cloud porosity.* While mass PDFs are well fit by lognormals in the circumcluster surface density  $\Sigma^c$  (see e.g., Figure 6), the solid-angle PDF is lognormal only at high  $\Sigma^c$ . This implies that the optical depth to UV radiation is less than unity over most of the sky (e.g., Figure 8), even in our highest surface density models. Over much of a cloud’s lifetime, 50% or more of the radiation can escape (see e.g., Figure 9, 10), rather than contributing to the driving of gaseous outflows.

Cumulatively, the absorption fraction is 50%–80% at 3 Myr after star formation begins (when the first SNe would explode), and 30%–60% after 8 Myr (when the luminosity would drop to half its original value). These results apply across clouds of all surface densities: clouds with higher surface density absorb more radiation at coeval stages in their evolution, but they also have shorter freefall times and therefore evolve more rapidly compared to the stellar evolution time. Because higher- $\Sigma_{\text{cl}}$  clouds have higher SFE, clusters that form within these clouds would contribute proportionally more to the ambient UV radiation field within galaxies.

If  $\sigma_{\ln \Sigma}$  is lower in real clouds than in our simulations, it would tend to reduce the escape of radiation.

4. *Gas outflows.* We find that the mean velocity (or momentum/mass) of outflowing gas in our simulations ranges over  $\sim (1.5\text{--}2.5)v_{\text{esc}}(r_{\text{cl},0})$  (see Figure 11). Figure 14 shows that the mean velocity of the outflow increases secularly with cloud mass.

We also consider the relationships between velocity and circumcluster surface density in our models, as well as the distribution of mass with velocity. We are able to interpret both of these relationships in terms of an essentially “ballistic” model for ejection of structures by radiation forces, with the velocity-surface density relationship given by Equation (15). Regions with lower surface density are preferentially driven to higher velocity and evidently remain coherent long enough to match the expected relationship (see Figure 13).

The distribution of mass as a function of velocity for outflowing gas (Figure 12) extends to velocities well above the escape speed  $\sim v_{\text{esc}}$  from the surface of the

cloud. A lognormal distribution of mass as a function of  $\Sigma^c$  at a given launch radius maps to a distribution of mass versus velocity at the outer edge of the simulation domain. The overall mass-velocity relationship can then be understood as the superposition of distributions of material launched from a range of radii within the cloud with a known radial density profile (see Figure 13). The high-velocity tail originates deepest in the potential well and experiences the strongest radiation forces.

Equation (16) shows that at large distance from the launch point  $r_0$ , optically thin structures would reach  $\sim 9v_{\text{esc}}(r_0)$ , while structures that are marginally Eddington would reach  $\sim 3.7v_{\text{esc}}(r_0)$ . These velocities are a few to several tens of  $\text{km s}^{-1}$  for the clouds and clusters we consider. However, Thompson & Krumholz (2016) suggest that a similar dynamical process of radiative cloud acceleration may also hold in extreme starburst systems with high  $v_{\text{esc}}$ , in which case the line profiles of high-velocity cool gas could be calculated using a similar formalism to that given here, as expressed in Equation (17).

Finally, we reiterate that the numerical simulations analyzed here are idealized in several respects, and in this sense are best thought of as controlled numerical experiments rather than comprehensive models of real clouds. As such, this study provides for the first time a systematic investigation of the radiation-matter interaction in turbulent, self-gravitating, uniformly cold, unmagnetized clouds with localized collapse and UV feedback, which can be the basis for future studies with more comprehensive physics.

We are grateful to the referee for a thorough and insightful report. This work was supported by grant No. AST-1312006 from the National Science Foundation. M.A.S. was supported by the Max Planck/Princeton Center for Plasma Astrophysics under grant NSF PHY-1144374. Part of this project was conducted during a visit to the KITP at U.C. Santa Barbara, which is supported by the National Science Foundation under grant No. NSF PHY11-25915. Simulations were performed on the computational resources supported by the PICSciE TIGRESS High Performance Computing Center at Princeton University.

## ORCID iDs

Eve C. Ostriker  <https://orcid.org/0000-0002-0509-9113>

## References

- Adams, F. C. 2000, *ApJ*, **542**, 964
- André, P., Di Francesco, J., Ward-Thompson, D., et al. 2014, in *Protostars and Planets VI*, ed. H. Beuther et al. (Tucson, AZ: Univ. Arizona Press), 27
- Ballesteros-Paredes, J., Vázquez-Semadeni, E., Gazol, A., et al. 2011, *MNRAS*, **416**, 1436
- Banerjee, R., Vázquez-Semadeni, E., Hennebelle, P., & Klessen, R. S. 2009, *MNRAS*, **398**, 1082
- Baumgardt, H., & Kroupa, P. 2007, *MNRAS*, **380**, 1589
- Boily, C. M., & Kroupa, P. 2003, *MNRAS*, **338**, 665
- Brunt, C. M., Federrath, C., & Price, D. J. 2010, *MNRAS*, **403**, 1507
- Bunker, A. J., Wilkins, S., Ellis, R. S., et al. 2010, *MNRAS*, **409**, 855
- Butler, M. J., Tan, J. C., & Kainulainen, J. 2014, *ApJL*, **782**, L30
- Chevalier, R. A., & Clegg, A. W. 1985, *Natur*, **317**, 44
- Colín, P., Vázquez-Semadeni, E., & Gómez, G. C. 2013, *MNRAS*, **435**, 1701
- Collins, D. C., Kritsuk, A. G., Padoan, P., et al. 2012, *ApJ*, **750**, 13
- Dale, J. E., Bonnell, I. A., Clarke, C. J., & Bate, M. R. 2005, *MNRAS*, **358**, 291
- Dale, J. E., Ercolano, B., & Bonnell, I. A. 2012, *MNRAS*, **424**, 377
- Dale, J. E., Ercolano, B., & Bonnell, I. A. 2013, *MNRAS*, **430**, 234
- Da Rio, N., Tan, J. C., & Jaehnig, K. 2014, *ApJ*, **795**, 55
- Davis, S. W., Jiang, Y.-F., Stone, J. M., & Murray, N. 2014, *ApJ*, **796**, 107
- Dekel, A., & Krumholz, M. R. 2013, *MNRAS*, **432**, 455
- Dobbs, C. L., Krumholz, M. R., Ballesteros-Paredes, J., et al. 2013, in *Protostars and Planets VI*, ed. H. Beuther et al. (Tucson, AZ: Univ. Arizona Press), 3
- Dopita, M. A., Fischera, J., Sutherland, R. S., et al. 2006, *ApJ*, **647**, 244
- Draine, B. T. 2011, *ApJ*, **732**, 100
- Elmegreen, B. G. 1983, *MNRAS*, **203**, 1011
- Elmegreen, B. G., & Scalo, J. 2004, *ARA&A*, **42**, 211
- Fall, S. M., Krumholz, M. R., & Matzner, C. D. 2010, *ApJL*, **710**, L142
- Faucher-Giguère, C.-A., Lidz, A., Hernquist, L., & Zaldarriaga, M. 2008, *ApJ*, **688**, 85
- Federrath, C., Banerjee, R., Clark, P. C., & Klessen, R. S. 2010, *ApJ*, **713**, 269
- Federrath, C., & Klessen, R. S. 2013, *ApJ*, **763**, 51
- Federrath, C., Klessen, R. S., & Schmidt, W. 2008, *ApJL*, **688**, L79
- Franx, M., Illingworth, G. D., Kelson, D. D., van Dokkum, P. G., & Tran, K.-V. 1997, *ApJL*, **486**, L75
- Geyer, M. P., & Burkert, A. 2001, *MNRAS*, **323**, 988
- Gnedin, N. Y., & Abel, T. 2001, *NewA*, **6**, 437
- Goldbaum, N. J., Krumholz, M. R., Matzner, C. D., & McKee, C. F. 2011, *ApJ*, **738**, 101
- Gong, H., & Ostriker, E. C. 2013, *ApJS*, **204**, 8
- Goodman, A. A., Pineda, J. E., & Schnee, S. L. 2009, *ApJ*, **692**, 91
- Goodwin, S. P. 1997, *MNRAS*, **284**, 785
- Goodwin, S. P., & Bastian, N. 2006, *MNRAS*, **373**, 752
- Harwit, M. 1962, *ApJ*, **136**, 832
- Heckman, T. M., Armus, L., & Miley, G. K. 1990, *ApJS*, **74**, 833
- Heyer, M., & Dame, T. M. 2015, *ARA&A*, **53**, 583
- Hockney, R. W., & Eastwood, J. W. 1981, *Computer Simulation Using Particles* (New York: McGraw-Hill)
- Hoopes, C. G., & Walterbos, R. A. M. 2000, *ApJ*, **541**, 597
- Hopkins, P. F., Quataert, E., & Murray, N. 2011, *MNRAS*, **417**, 950
- Hopkins, P. F., Quataert, E., & Murray, N. 2012, *MNRAS*, **421**, 3488
- Iffrig, O., & Hennebelle, P. 2015, *A&A*, **576**, A95
- Kainulainen, J., Beuther, H., Henning, T., & Plume, R. 2009, *A&A*, **508**, L35
- Kim, C.-G., & Ostriker, E. C. 2015, *ApJ*, **802**, 99
- Kim, J.-G., Kim, W.-T., & Ostriker, E. C. 2016, *ApJ*, **819**, 137
- Kim, J. G., Kim, W.-T., & Ostriker 2017, *ApJ*, in press
- Klessen, R. S., Heitsch, F., & Mac Low, M.-M. 2000, *ApJ*, **535**, 887
- Kritsuk, A. G., Norman, M. L., & Wagner, R. 2011, *ApJL*, **727**, L20
- Krumholz, M. R., & Dekel, A. 2010, *MNRAS*, **406**, 112
- Krumholz, M. R., Klein, R. I., McKee, C. F., & Bolstad, J. 2007, *ApJ*, **667**, 626
- Krumholz, M. R., & Matzner, C. D. 2009, *ApJ*, **703**, 1352
- Krumholz, M. R., & Thompson, T. A. 2012, *ApJ*, **760**, 155
- Krumholz, M. R., & Thompson, T. A. 2013, *MNRAS*, **434**, 2329
- Kuhlen, M., & Faucher-Giguère, C.-A. 2012, *MNRAS*, **423**, 862
- Lada, C. J., & Lada, E. A. 2003, *ARA&A*, **41**, 57
- Lada, C. J., Margulis, M., & Dearborn, D. 1984, *ApJ*, **285**, 141
- Larson, R. B. 1969, *MNRAS*, **145**, 271
- Lee, E. J., Chang, P., & Murray, N. 2015, *ApJ*, **800**, 49
- Levermore, C. D. 1984, *JQSRT*, **31**, 149
- Lim, W., Tan, J. C., Kainulainen, J., Ma, B., & Butler, M. J. 2016, *ApJL*, **829**, L19
- Lombardi, M., Alves, J., & Lada, C. J. 2015, *A&A*, **576**, L1
- Lombardi, M., Lada, C. J., & Alves, J. 2010, *A&A*, **512**, A67
- Longmore, S. N., Kruijssen, J. M. D., Bastian, N., et al. 2014, in *Protostars and Planets VI*, ed. H. Beuther et al. (Tucson, AZ: Univ. Arizona Press), 291
- Lopez, L. A., Krumholz, M. R., Bolatto, A. D., et al. 2014, *ApJ*, **795**, 121
- Lopez, L. A., Krumholz, M. R., Bolatto, A. D., Prochaska, J. X., & Ramirez-Ruiz, E. 2011, *ApJ*, **731**, 91
- Mac Low, M.-M., & Klessen, R. S. 2004, *RvMP*, **76**, 125
- Madau, P., Haardt, F., & Rees, M. J. 1999, *ApJ*, **514**, 648
- Martin, C. L. 2005, *ApJ*, **621**, 227
- Martizzi, D., Faucher-Giguère, C.-A., & Quataert, E. 2015, *MNRAS*, **450**, 504
- Matzner, C. D. 2002, *ApJ*, **566**, 302
- Matzner, C. D., & Jumper, P. H. 2015, *ApJ*, **815**, 68
- McKee, C. F., & Ostriker, E. C. 2007, *ARA&A*, **45**, 565
- McKee, C. F., & Tan, J. C. 2003, *ApJ*, **585**, 850
- Ménard, B., Wild, V., Nestor, D., et al. 2011, *MNRAS*, **417**, 801
- Murray, N. 2011, *ApJ*, **729**, 133
- Murray, N., Quataert, E., & Thompson, T. A. 2005, *ApJ*, **618**, 569
- Murray, N., Quataert, E., & Thompson, T. A. 2010, *ApJ*, **709**, 191
- O'Dell, C. R., York, D. G., & Henize, K. G. 1967, *ApJ*, **150**, 835

- Olsen, K. P., Greve, T. R., Brinch, C., et al. 2016, *MNRAS*, 457, 3306
- Ostriker, E. C., & Shetty, R. 2011, *ApJ*, 731, 41
- Ostriker, E. C., Stone, J. M., & Gammie, C. F. 2001, *ApJ*, 546, 980
- Padoan, P., Jimenez, R., Juvela, M., & Nordlund, Å. 2004a, *ApJL*, 604, L49
- Padoan, P., Jimenez, R., Nordlund, Å., & Boldyrev, S. 2004b, *PhRvL*, 92, 191102
- Pellegrini, E. W., Baldwin, J. A., Brogan, C. L., et al. 2007, *ApJ*, 658, 1119
- Pellegrini, E. W., Baldwin, J. A., & Ferland, G. J. 2010, *ApJS*, 191, 160
- Penston, M. V. 1969, *MNRAS*, 144, 425
- Pettini, M., Shapley, A. E., Steidel, C. C., et al. 2001, *ApJ*, 554, 981
- Pettini, M., Steidel, C. C., Adelberger, K. L., Dickinson, M., & Giavalisco, M. 2000, *ApJ*, 528, 96
- Pfalzner, S., Kirk, H., Sills, A., et al. 2016, *A&A*, 586, A68
- Plummer, H. C. 1911, *MNRAS*, 71, 460
- Price, D. J., Federrath, C., & Brunt, C. M. 2011, *ApJL*, 727, L21
- Proszkow, E.-M., & Adams, F. C. 2009, *ApJS*, 185, 486
- Raskutti, S., Ostriker, E. C., & Skinner, M. A. 2016, *ApJ*, 829, 130
- Roman-Duval, J., Jackson, J. M., Heyer, M., Rathborne, J., & Simon, R. 2010, *ApJ*, 723, 492
- Rupke, D. S., Veilleux, S., & Sanders, D. B. 2005, *ApJS*, 160, 115
- Sales, L. V., Marinacci, F., Springel, V., & Petkova, M. 2014, *MNRAS*, 439, 2990
- Scannapieco, E., & Brügggen, M. 2015, *ApJ*, 805, 158
- Schneider, N., André, P., Könyves, V., et al. 2013, *ApJL*, 766, L17
- Schneider, N., Ossenkopf, V., Csengeri, T., et al. 2015, *A&A*, 575, A79
- Scoville, N. 2003, *JKAS*, 36, 167
- Scoville, N. Z., Polletta, M., Ewald, S., et al. 2001, *AJ*, 122, 3017
- Scoville, N. Z., & Solomon, P. M. 1975, *ApJL*, 199, L105
- Scoville, N. Z., Yun, M. S., Sanders, D. B., Clemens, D. P., & Waller, W. H. 1987, *ApJS*, 63, 821
- Shapley, A. E., Steidel, C. C., Pettini, M., & Adelberger, K. L. 2003, *ApJ*, 588, 65
- Skinner, M. A., & Ostriker, E. C. 2013, *ApJS*, 206, 21
- Skinner, M. A., & Ostriker, E. C. 2015, *ApJ*, 809, 187
- Springel, V. 2005, *MNRAS*, 364, 1105
- Steidel, C. C., Giavalisco, M., Pettini, M., Dickinson, M., & Adelberger, K. L. 1996, *ApJL*, 462, L17
- Stone, J. M., & Gardiner, T. 2009, *NewA*, 14, 139
- Stone, J. M., Gardiner, T. A., Teuben, P., Hawley, J. F., & Simon, J. B. 2008, *ApJS*, 178, 137
- Stone, J. M., Ostriker, E. C., & Gammie, C. F. 1998, *ApJL*, 508, L99
- Thompson, T. A., Fabian, A. C., Quataert, E., & Murray, N. 2015, *MNRAS*, 449, 147
- Thompson, T. A., & Krumholz, M. R. 2016, *MNRAS*, 455, 334
- Thompson, T. A., Quataert, E., & Murray, N. 2005, *ApJ*, 630, 167
- Thompson, T. A., Quataert, E., Zhang, D., & Weinberg, D. H. 2016, *MNRAS*, 455, 1830
- Tremonti, C. A., Moustakas, J., & Diamond-Stanic, A. M. 2007, *ApJL*, 663, L77
- Vázquez-Semadeni, E., Banerjee, R., Gómez, G. C., et al. 2011, *MNRAS*, 414, 2511
- Vázquez-Semadeni, E., Colín, P., Gómez, G. C., Ballesteros-Paredes, J., & Watson, A. W. 2010, *ApJ*, 715, 1302
- Vázquez-Semadeni, E., & García, N. 2001, *ApJ*, 557, 727
- Vázquez-Semadeni, E., González, R. F., Ballesteros-Paredes, J., Gazol, A., & Kim, J. 2008, *MNRAS*, 390, 769
- Veilleux, S., Cecil, G., & Bland-Hawthorn, J. 2005, *ARA&A*, 43, 769
- Voges, E. S., & Walterbos, R. A. M. 2006, *ApJL*, 644, L29
- Walch, S., & Naab, T. 2015, *MNRAS*, 451, 2757
- Walch, S. K., Whitworth, A. P., Bisbas, T., Wünsch, R., & Hubber, D. 2012, *MNRAS*, 427, 625
- Wang, B. 1995, *ApJ*, 444, 590
- Weiner, B. J., Coil, A. L., Prochaska, J. X., et al. 2009, *ApJ*, 692, 187
- Weingartner, J. C., & Draine, B. T. 2001, *ApJ*, 548, 296
- Whitworth, A. P., & Ward-Thompson, D. 2001, *ApJ*, 547, 317
- Zhang, D., & Thompson, T. A. 2012, *MNRAS*, 424, 1170